
Masters Theses

Student Theses and Dissertations

Summer 2016

Design and fabrication of a system for the additive manufacturing of transparent glass

Luke John Gilbert

Follow this and additional works at: https://scholarsmine.mst.edu/masters_theses



Part of the [Mechanical Engineering Commons](#)

Department:

Recommended Citation

Gilbert, Luke John, "Design and fabrication of a system for the additive manufacturing of transparent glass" (2016). *Masters Theses*. 7738.

https://scholarsmine.mst.edu/masters_theses/7738

This thesis is brought to you by Scholars' Mine, a service of the Missouri S&T Library and Learning Resources. This work is protected by U. S. Copyright Law. Unauthorized use including reproduction for redistribution requires the permission of the copyright holder. For more information, please contact scholarsmine@mst.edu.

DESIGN AND FABRICATION OF A SYSTEM FOR THE ADDITIVE
MANUFACTURING OF TRANSPARENT GLASS

by

LUKE JOHN GILBERT

A THESIS

Presented to the Faculty of the Graduate School of the
MISSOURI UNIVERSITY OF SCIENCE AND TECHNOLOGY

In Partial Fulfillment of the Requirements for the Degree

MASTER OF SCIENCE IN MECHANICAL ENGINEERING

2016

Approved by

Edward C. Kinzel
Douglas A. Bristow
Robert G. Landers

© 2016

Luke John Gilbert
All Rights Reserved

ABSTRACT

Despite glass' prevalence in the scientific and engineering community, very little research has been conducted attempting to additively manufacture (AM) glass. Even less research has been done on optically transparent glass. Glass' material properties make it ineligible for most AM processes if the end result is to be transparent. Even small gas inclusions can cause large amounts of scattering. Additively manufacturing transparent glass brings the advantages found in other AM processes with the added benefit of having optical properties better than those found in polymers. Additively manufacturing glass also allows the optical properties of transparent parts to vary arbitrarily. This thesis presents the design, manufacture, and control of a system to AM transparent glass. The system feeds glass wires, which are opaque in the near infrared, into a melt pool maintained by a CO₂ laser (10.6 μ m). The laser beam and melt pool remained fixed as the AM part is moved using a motion stage as the glass is deposited layer-by-layer. The stages are controlled using a PID controller, and the wire feeders are controlled using a PD controller. A spring damper model is also presented to model the deposition process along the feed direction, and perpendicular to the feed direction for control purposes. The Glass AM process is able to create morphologically accurate glass pieces more efficiently, and with fewer filament breakages than the prototype system. The glass produced with this system has optical properties as good as cast glass. The Glass AM system is also expandable and interchangeable so that more subsystems can be added and changed with minimal redesign.

ACKNOWLEDGMENTS

I would like to thank my advisers, Drs. Bristow, Landers, and Kinzel, for their guidance and help through these last two years. They taught me more than I knew I didn't know. I would also like to thank Ben Sprouse, Brian Bullock, Joe Boze, and Mitch Cottrell, for helping me build the Glass AM machine, and answering all my stupid questions.

I'd like to thank Patrick Sammons, Muthu Loganathan, Hesam Zomoradi, Nima Yagin, and all the other grad students for helping me out when I ran into problems. I'd like to thank Patrick Bazzoli, Le Ma, Navid Rezazadeh, and Michelle Gegel for all of the fun times, help with homework, and strange conversations.

I'd like to thank Junjie Luo for all the work he's done on Glass AM, and for keeping me company during the long work nights, along with Chuang Qu, Qizi Zhang, and Tao Liu. I'd also like to thank Warren Vaz for all the advice on life and grad school and interesting lunch conversations.

I'd like to thank the National Science Foundation (NSF CMMI-1538464), the Department of Education (DOE grant P200 A120062), and the Intelligent Systems Center (ISC) for funding me, without which I would not have been able to go to graduate school.

Last but not least, I'd like to thank my parents, Jeff and Shari, and my siblings, Becca and Daniel, for supporting me throughout my grad school career. I'd like to thank all my friends, specifically the guys and gals at the Brick House and House of Nine, who kept me sane.

TABLE OF CONTENTS

	Page
ABSTRACT.....	iii
ACKNOWLEDGMENTS	iv
LIST OF ILLUSTRATIONS.....	vii
LIST OF TABLES.....	ix
 SECTION	
1. INTRODUCTION.....	1
1.1. LITERATURE REVIEW AND MOTIVATIONS.....	1
1.2. PROTOTYPE SYSTEM.....	4
1.2.1. Mechanical Systems.....	4
1.2.2. Optical Systems.....	6
1.2.3. Electrical Systems.....	7
1.2.4. Software Systems.....	7
1.3. PROTOTYPE SYSTEM DESIGN FLAWS	8
1.4. GLASS AM DESIGN GOALS	10
2. SYSTEM OVERVIEW	13
2.1. MECHANICAL SYSTEMS.....	13
2.1.1. Wire Feeders.....	13
2.1.2. Motion Stages and Substrate Heater.....	19
2.2. OPTICAL SYSTEMS.....	21
2.3. ELECTRICAL SYSTEMS.....	26
2.4. SOFTWARE SYSTEMS.....	32

3. SYSTEM CONTROL	35
3.1. WIRE FEEDER CONTROLLERS.....	35
3.2. AEROTECH STAGE CONTROLLERS.....	37
4. PROCESS MODELING	42
5. RESULTS AND ANALYSIS	49
6. SUMMARY AND CONCLUSION.....	55
7. FUTURE WORK AND LIMITATIONS.....	57
APPENDICES	
A. PATH GENERATION CALCULATIONS.....	60
B. ERROR HANDLING.....	70
BIBLIOGRAPHY.....	74
VITA.....	78

LIST OF ILLUSTRATIONS

	Page
Figure 1.1. Glass AM Prototype System Without the Prototype Wire Feeder Mounted	5
Figure 1.2. A Front and Side View of the Wire Feeding Mechanism.	6
Figure 1.3. The Bottom Half of a Wire Feeder after Overheating.....	8
Figure 2.1. Photograph Showing the Clamping Action Used in a TIG Welder Wire Feeder	14
Figure 2.2. New Wire Feeders as Viewed from the Top and Bottom Respectively.....	16
Figure 2.3. An Exploded View of the Wire Feeder Clamping Mechanism.....	17
Figure 2.4. Isometric View of the Wire Guide..	18
Figure 2.5. The Mounted Wire Feeders and the Unobstructed Optical path of the CO ₂ Laser	20
Figure 2.6. Aerotech Stages used in the Glass AM Process with the Substrate heater attached.....	21
Figure 2.7. The Substrate Heater with a Soda-Lime Glass Slide Bolted Into Place on the Build Platform.	22
Figure 2.8. Optical Systems Diagram.	24
Figure 2.9. The Spectral Emission of the Glass AM System at Various Laser Powers, with a Constant Scan Speed.	25
Figure 2.10. Glass AM Electrical Cabinet.....	27
Figure 2.11. Glass AM Electrical Cabinet Wiring Schematic.....	29
Figure 2.12. Glass AM Electrical Signal Wiring.....	31
Figure 2.13. Software Systems Hierarch Block Diagram.....	34
Figure 3.1. Velocity Response of a Single Revolution of a Yaskawa Motor to a Constant Voltage Input with a 100 Hz Dithering Signal.	36

Figure 3.2. Velocity Response of a Wire Feeder Tuned with a PI controller with the gains 0.01 and 1.7 respectively.	36
Figure 3.3. Position Plot of the test shown in Figure 3.2.....	37
Figure 3.4. X Stage Response to a Square Wave.....	39
Figure 3.5. X Stage Response to a Ramp Function	39
Figure 3.6. Z Stage Response to a Square Wave	40
Figure 3.7. Z Stage Response to a Ramp Function.....	40
Figure 3.8. Y Stage Response to a Square Wave.....	41
Figure 3.9. Y Stage Response to a Ramp Function	41
Figure 4.1. Commonly Used Temperatures in Glass Manufacturing for Soda-Lime Glass [35]—Reproduced by permission of The Royal Society of Chemistry.....	43
Figure 4.2. Schematic Detailing the Physics of the Glass AM Process.....	44
Figure 4.3. Equivalent Massless Spring Damper Model	45
Figure 4.4. Rotated View of the Glass AM Deposition Process.....	48
Figure 4.5. Equivalent Massless Spring Damper in the Direction Perpendicular to the Feeding Direction	48
Figure 5.1. Wall Made with Prototype System and Hand Feeding on the Left, and Two Walls Printed on the New Glass AM system on the Right.....	53
Figure 5.2. 3D Printed Soda-Lime Glass Pyramid.	54

LIST OF TABLES

	Page
Table 2.1. The dimensions of the interchangeable parts in the wire feeder needed to feed different diameter wires.....	18
Table 5.1. The Worst Case Deflection Calculations for the Prototype Wire Feeder.....	50
Table 5.2. The Worst Case Deflection Calculations for the New Wire Feeder.....	50
Table 5.3. Average Feeder Velocity Response to a Reference Velocity.....	51
Table 5.4. Aerotech Stage Controller Response	52

1. INTRODUCTION

1.1. LITERATURE REVIEW AND MOTIVATIONS

As additive manufacturing (AM) has grown in popularity, its utility has been proven time and time again. With its ability to rapidly produce prototypes from Computer Aided Design (CAD) models and quickly and cheaply complete small scale production runs, it has become a staple of the modern design process. Until recently, most of the work done in the AM field has been focused on the AM of structural components.

The lack of research into transparent materials overlooks a unique opportunity to create gradient index (GRIN) optics and transformation optics (TO). The leap to additive manufacturing GRIN lenses is the next logical step from polymerization [1]. Current methods of producing GRIN optics are time consuming, expensive, and the index profiles that are created are extremely limited in both change of index and geometry. AM of transparent parts with varying indexed materials would allow arbitrary control of local indices of refraction and ultimately the creation of GRIN optics and TO.

The current state of the art of transparent AM is focused mainly on polymers as AM processes exist for polymers. While not necessarily in the pursuit of GRIN and TO optics, transparent AM polymer parts have been created using Selective Laser Sintering (SLS) [2], Multiphoton Stereolithography (SLM) [3], Multi-jet modeling [4,5], and Fused Deposition Modeling (FDM) [6]. Ink jet printing with in-situ UV curing has even been used to create gradient index lenses by changing the index of refraction layer-by-layer [7]. While these processes produce low-cost, low-power polymer optics, and toys [8,9] they are unable to be used in high precision, high-power optics. Plastics have relatively

low transmissivity and thermally unstable indices. For high power optics, glasses are necessary [10].

Surprisingly little work has been done on the AM of glass even less has been done on the AM of transparent glass. Of the 7 types of AM processes recognized by the ASTM F42 committee, [11] only two of these processes have been used in literature to additively manufacture glass.

Powdered processes have been used to print glasses and ceramics [12-15]. These methods have yielded morphologically accurate parts, but the parts that they have produced have significant gas inclusions in them. As shown in Pilon et. al., even small gas inclusions can cause large scattering of light [16,17]. This scattering effect renders powder processes inviable for optical uses. Blown powder processes similar to Laser Metal Deposition (LMD) or Electron Beam AM (EBAM) also tend to trap atmospheric gasses. Similarly, these processes, too, are unable to create transparent parts. Klein et al. have also pursued a novel powder based process where glass is melted using extreme currents in methods deemed “direct spark sintering” and “Lichtenberg sintering”. The pieces produced using these methods have large gas inclusions rendering them opaque [18].

Binder Jetting has been successfully used to 3D print Glass using maltodextrin and indexed matched polysaccharide as a binder [19,20]. These binders were burnt out during the firing process, but the presence of the binder along with the spacing between the frit, created gas inclusions and left the samples at an estimated density of 60% [19]. Similarly, Vat photopolymerization and material jetting would also cause gas inclusions

when the material binding the frit was burnt off rendering them ineligible as processes able to produce transparent glass parts.

While there has been some success with the extrusion of molten glasses [18], this process too seems to be limited to large builds. The literature has shown that powder based processes and binder based processes will not be able to produce transparent parts. As an alternative to powder and binder processes, wire fed processes were investigated as a means to AM transparent glass. Wire fed processes waste less material and are less likely to be contaminated than powder based processes. Parts created using wire fed processes have mechanical properties comparable to cast parts and, unlike binder based processes, are fully dense [21-23]. A large body of literature is present documenting optimal parameters for wire fed processes including the wire angle and feed direction [24,25]. Height and stability control have been documented [23, 26, 27], and micro scale parts have even been produced [28].

With metal wire fed processes as the inspiration, a novel glass wire fed process was created [29, 30]. This process uses fully dense glass filaments or wires. The glass filament is fed into a melt pool maintained by a CO₂ laser as a set of stages moves the substrate about the fixed focus of the laser. Once one layer has been deposited, the next layer is deposited on top of the previous layer creating fully dense transparent glass parts. This process has been repeated with soda-lime [29, 30], quartz [31, 32], borosilicate glass, flint glass, and alumina. When measured, the optical properties of soda-lime, and quartz are as good as cast glasses [29-32].

1.2. PROTOTYPE SYSTEM

The Glass AM prototype system was composed of four systems: the mechanical systems, the optical systems, the electrical systems, and the software systems. The mechanical systems provide motion to the system, the optical systems monitor, supply and manipulate electromagnetic energy inside the system, the electrical systems contain the hardware which monitors the prototype system and computes the control software, and the software systems contain the user interfaces and control algorithms that govern the process. Figure 1.1. shows the prototype system.

1.2.1. Mechanical Systems. The mechanical systems consisted of the X and Y stages (Thorlabs DDSM100) with a scissor type lab jack Z stage (Thorlabs L490MZ), a generic electric strip heater, a custom 3D printed wire feeder, and a bipolar stepper motor (Pololu 1208).

The stages were composed of two direct drive linear axes and one stepper motor driven lab scissor jack. The X and Y positions depended upon the linear axes and the Z position depended upon the screw jack. The stages had a range of 100mm for the X and Y axis with a resolution of 500nm, while Z stage had a range of 50 mm and a resolution of 20nm. The stages were capable of a velocity of up to 500mm/s, though depending upon the load, there was a risk of overcurrent above speeds of 100mm/s. The maximum acceleration in the X and Y directions was 5000mm/s^2 . The maximum acceleration in the Z direction was 0.25 mm/s^2 . Normal operating accelerations were 500mm/s^2 for the X and Y stages, and 0.25mm/s^2 for the Z stage.

Attached to the stages was a strip heater. This strip heater acted as a substrate heater and helped to alleviate the thermal stresses induced by the AM process.



Figure 1.1. Glass AM Prototype System Without the Prototype Wire Feeder Mounted.

It was powered by a 125V 1A source, and could reach 550°C. Material was fed into the melt pool using custom designed 3D-printed thermoplastic wire feeders, shown in Figure 1.2.

These wire feeder bodies consisted of two parts: a top and bottom piece that clamp down on glass filaments using 3-D printed wheels with a 0.25mm groove in them. The pressure was kept on the filaments by threading two shoulder bolts through two springs, and screwing the shoulder bolts into tapped holes in the bottom thermoplastic piece. The movement of the wheels was provided by a 10V 0.5A bipolar stepper motor with 200 steps per revolution and a holding torque of 14 oz*in (0.099 N*M).



Figure 1.2. A Front and Side View of the Wire Feeding Mechanism. The bottom left wheel is powered by a bipolar stepper motor and the top piece is held in place by two shoulder bolts which are screwed into tapped holes in the thermoplastic bottom piece. The picture on the right shows the wire feeder rotated 90 degrees to show the mounting mechanism, the hole through which glass was fed, and the groove in the wheels.

1.2.2. Optical Systems. The optical systems consisted of two lasers and the Ophir 10A-V1.1 power meter. The first laser was a 100 milliwatt Helium-Neon laser ($\lambda_0 = 635\text{nm}$), and the second, a 100 watt GEM-100 air cooled industrial CO_2 laser ($\lambda_0 = 10.5\mu\text{m}$).

The first laser, the Melles Griot 100 milliwatt Helium-Neon was combined with the CO_2 laser to provide a visual reference for the actual position of the GEM-100 Air Cooled Industrial Laser as the CO_2 laser is not in the visible spectrum. Its main purpose was for assisting in alignment of the laser and glass pieces and to act as a safety mechanism.

The second laser, the GEM-100 Air Cooled Industrial Laser, was a 100 W laser, maintained the melt pool of the Glass AM process by supplying electromagnetic energy.

It was controlled using a custom made controller with no read out of the power supplied to the laser or by the laser.

An Ophir 10A-V1.1 power meter was used to measure the power of a laser. As the Ophir 10A-V1.1 is a thermopile sensor capable of sensing powers up to 10 Watts, 1% of the laser's power was split from the CO₂ laser to be read by the power meter.

1.2.3. Electrical Systems. The electrical systems were composed of a personal computer running LabVIEW 2013, a NI myDAQ, and two TBD001 T-Cube Brushless Servo Drivers, and a stepper motor controller (Big Easy Driver Stepper Motor Controller RB-Ite-131). The personal computer handled all of the control processes with a LabVIEW program and contained the Graphical User Interface (GUI). The NI myDAQ acted as a digital output device which signaled the stepper motor controller when to move forward a step. The motor stepper controller takes a 5 volt digital A and B phase signal and outputs a 10 volt signal to advance the motor. The TBD001 T-Cub Brushless drivers controlled the X and Y stages position; an internal controller had the same function for the Z stage.

1.2.4. Software Systems. The prototype Glass AM prototype process were controlled using a custom LabVIEW program. The LabVIEW program interfaced with the Thorlab stages via the stages proprietary LabVIEW drivers. The Thorlabs controllers used a PID to control position, and used a trapezoidal velocity profile for its reference generation.

The stepper motors were controlled by switching on and off the digital lines to the stepper motor controller in an open loop fashion. The path planning of the stages and motor speed was controlled using a pseudo G-Code that commanded the final position of

the stages while estimating the time between the start of the command and when the final position was reached before updating the next position. The stages and feeder could also be moved in a “jog mode” where the position was updated using by a predetermined offset and where the feeder speed was able to be entered manually.

1.3. PROTOTYPE SYSTEM DESIGN FLAWS

While the prototype system showed that the Glass AM process could be automated, and could produce transparent optical quality glass, the morphology of the parts was subpar, and there was much room for improvement.

The wire feeder suffered from several problems. The first problem was that the wire feeders were made out of black thermoplastic and tended to melt when operated closer than 6cm from the melt pool. This was due to the extremely high temperature of the melt pool, measured in some cases at over 1800°C, and the relatively low melting temperature of 3D printed thermoplastic. An example of this is shown in Figure 1.3.

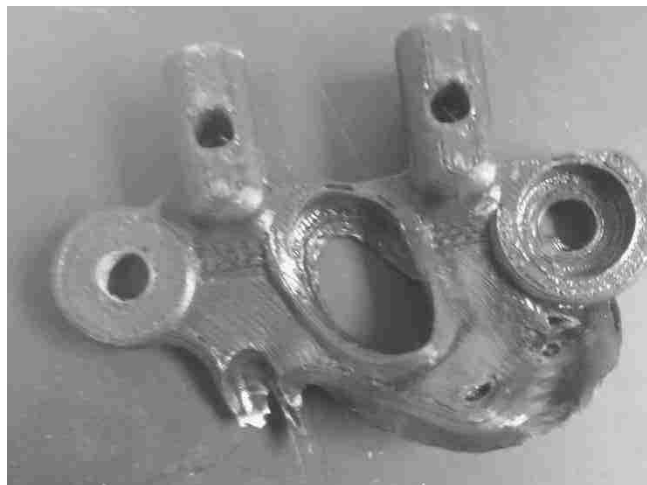


Figure 1.3. The Bottom Half of a Wire Feeder after Overheating.

The distance from the melt pool presented a second problem, while soda-lime glass has a high modulus of elasticity (70mpa[33]) and is very stiff, at 6cm a 1mm soda-lime filament will begin to show significant deflection, just from gravity. The deflection of the tip of the filament was even greater once the viscous force of the melt pool was exerted on the tip of the filament.

The wire feeders were also not robust to wire size. The wire feeders were only able to feed 0.5 mm and 1 mm wire. The wire feeder was not able to feed any wire larger or smaller due to the feeding channel size, and the size of the groove in the feeding wheels respectively.

The springs that were used to keep the wire feeders together had a spring constant far too large for the process, and the amount of force they generated was not able to be adjusted. They made feeding a new filament difficult, would tear out the tapped shoulder bolts, and crush the glass filaments. This would force the AM process to stop, often times mid build, and result in a failed part.

The wire feeders also tended to lock up as the force of the wire between the wheels exerted a rotational moment against the shoulder bolts that held the tensioning springs. This moment made separating the top and bottom pieces difficult when feeding in new wires.

The wire feeders were attached via a single bolt to an optical post. This gave the wire feeders an extra degree of rotational freedom that impeded alignment and limited the repeatability of the process between process runs.

The stepper motor also posed a problem. The stepper motor had a resolution of 1.8° and was run in open loop with a controller that limited the movement to 22.5° per

step. This stepper motor fed the wire into the melt pool in large jerky motions as the rotor moved from step to step. This limits the amount of control that can be had on the wire feeders, which is a severe limitation to the process.

The 100W GEM-100 CO₂ laser's power had to be tuned by hand by reading the output power from the power meter, before the process could be started. This added a significant time to the start of each build process. There was also no way to input a control signal to the laser. This meant that any change to the laser in the process had to be done manually. The laser was also not powerful enough to handle glasses like quartz, and ceramics like alumina.

The ThorLabs stages lacked the resolution, load capacity, and ability to implement advanced control techniques. All interfacing with the stages had to be done via their driver software which made tuning new controllers difficult. The controllers were tuned for a 250 g load, and the stage could handle a maximum load of 900 g. this meant that the size of the glass pieces that could be made and the types of heaters that could be mounted to the stages were severely limited.

The strip heater was a simple device, whose temperature lacked any ability to be controlled or observed, rendering it to be tuned heuristically for each process by adjusting the current supplied to it. While the strip heater is able to reach the annealing point of soda-lime glass, it was unable to be controlled or fixed to the stages.

1.4. GLASS AM DESIGN GOALS

In order to improve upon the prototype system, a set of design goals was created. The first goal is to design the wire feeders to operate as close to the melt pool as possible

to limit the amount of deflection in the wires. The smaller the deflection of the wires, the more accurate the process can be.

The second goal is to create a wire feeding mechanism that is able to feed wires between 2 mm borosilicate and 0.125 mm stripped single mode fiber optic cable. This is over a magnitude difference in size, and is important as the available diameter of various glass fibers is fairly limited. The system must be able to adapt not only to varying sizes but variations within the same wires.

The third goal is to create a wire feeding mechanism with variable tension springs to keep the filaments from breaking mid process. This goal goes hand in hand with a fourth goal, to create a system that allows new wires to be fed quickly and easily and doesn't lock up.

The fifth goal is to allow the wire feeder to be aligned with the laser and another wire feeder quickly, easily, and with a high repeatability, while eliminating any extra degrees of freedom.

The sixth goal is to incorporate a higher resolution motor for the wire feeders that are both observable and controllable.

The seventh goal is to incorporate a CO₂ laser that is capable of melting quartz and alumina, and is both observable and controllable with an analog signal or a PWM signal.

The eighth goal is to incorporate motion stages that have a high resolution and are able to be controlled using custom made controllers that can be incorporated into a process controller for future controls research.

The ninth goal is to incorporate a substrate heater whose temperature is able to be controllable and observable, as well as one able to connect directly to the stages.

The final goal is to create a more user friendly controlling program that cuts down the amount of time and setup necessary to create glass pieces.

2. SYSTEM OVERVIEW

The glass additive manufacturing process, like most modern processes, is composed of several distinct systems. These systems are split into four categories: the mechanical systems, the optical systems, the electrical systems, and the software systems. The mechanical systems are composed of the mechanical components that provide motion to the Glass AM process. The optics system's components supply electromagnetic energy into the process and observe any electromagnetic phenomena. The electrical systems are composed of the various electrical components needed to control the mechanical and optical systems. The software and control systems are composed of the software and control algorithms, which govern the process.

2.1. MECHANICAL SYSTEMS

The mechanical components used for Glass AM consist of two different subsystems, the wire feeders and the motion stages and build platform. The wire feeders translate the torque provided by servo motors into a linear filament feeding motion. It is the feeders that supply the material to the melt pool. The motion stages position the build platform where the work piece is created in three dimensional space. In order to keep thermal stresses from breaking AM workpieces, a substrate heater is attached to the stages and acts as the build platform.

2.1.1. Wire Feeders. The wire feeder was inspired from two sources, the previous iteration of wire feeders shown above in Figure 1.2. and the wire feeding mechanism in a TIG welder shown in Figure 2.1.

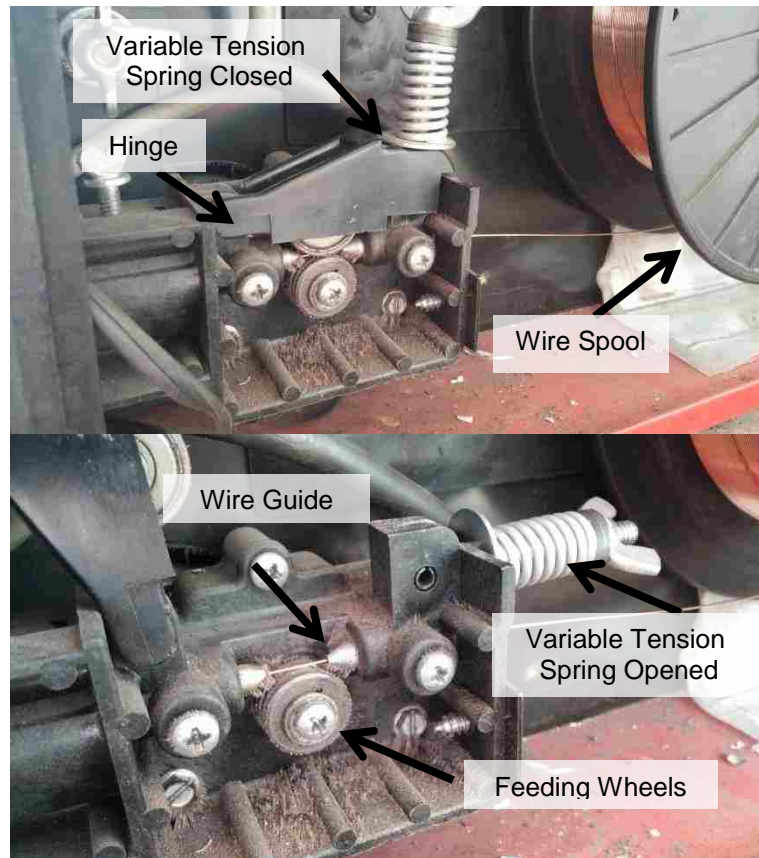


Figure 2.1. Photograph Showing the Clamping Action Used in a TIG Welder Wire Feeder.

The wire feeders are mechanisms that convert the rotational motion from a Yaskawa motors (SGMJV-01A3M61) to a linear motion of glass filaments into a laser generated melt pool. The Yaskawa Motors are 100 watt motors with a 20 bit encoder, operating at a resolution of 0.0027° degrees which translates into a resolution of $7\mu\text{m}$ of fed wire. This power is translated through anti backlash bevel gears (W.M. Berg, M48N-1-ABS) with 0.0985 ft. lbs. of preloaded torque to a set of two wheels, of which only one is powered. The contact between the two wheels and the wire is maintained through a 0.3 inch diameter “tensioning” spring, with a 1.4 lbs/in spring constant cut to 0.85 inches (McMaster-Carr, 9657K384) and attached via a $\frac{1}{4}$ x 20 bolt to a lever arm that contains

the unpowered wheel. The filament is fed through an exchangeable “wire feeding guide” by the mechanism and exits the end of the wire feeder through a pinch point created by a compliant spring and a custom made plate with a groove cut into it, which has been deemed the “feeder clamp”. A picture of the finished wire feeder is shown in Figure 2.2.

In order to decrease the amount of deflection in the glass filaments, the new wire feeders were designed to get as close to the melt pool as possible, and so were designed out of aluminum. Aluminum has a much higher melting point than ABS Thermoplastic, and its reflective surface doubles as a radiation shield against the radiative heat from the melt pool and substrate heater. As radiation is the dominant mode of heat transfer, this does a great deal to limit the transfer of heat from the melt pool to the wire feeder, and motor.

The two sets of wheels found in the prototype wire feeders were abandoned in order to get even closer to the melt pool. With two sets of wheels feeding the wire, the distance to the melt pool will always be limited by the radius of the front wheels. In order to get closer to the melt pool a clamping mechanism was created to replace the front set of wheels. This clamping mechanism uses a compliant spring made of 0.004” thick 1095 spring steel laser cut to size, a $\frac{1}{4}$ x 20 set screw and an aluminum clamping plate with a groove cut in it deemed the “Feeder Clamp”.

This mechanism allows the wire feeder to clamp down on the filament and prevent any transverse movement while allowing the wire to be fed into the melt pool at 10mm away from the melt pool. The wire feeder clamping mechanism is shown in Figure. 2.3. The feeder clamping mechanism, mentioned previously, along with the

tensioning spring, and wire guide allow filaments that range in diameter over an order of magnitude (2mm to .125mm) to be fed into the melt pool.

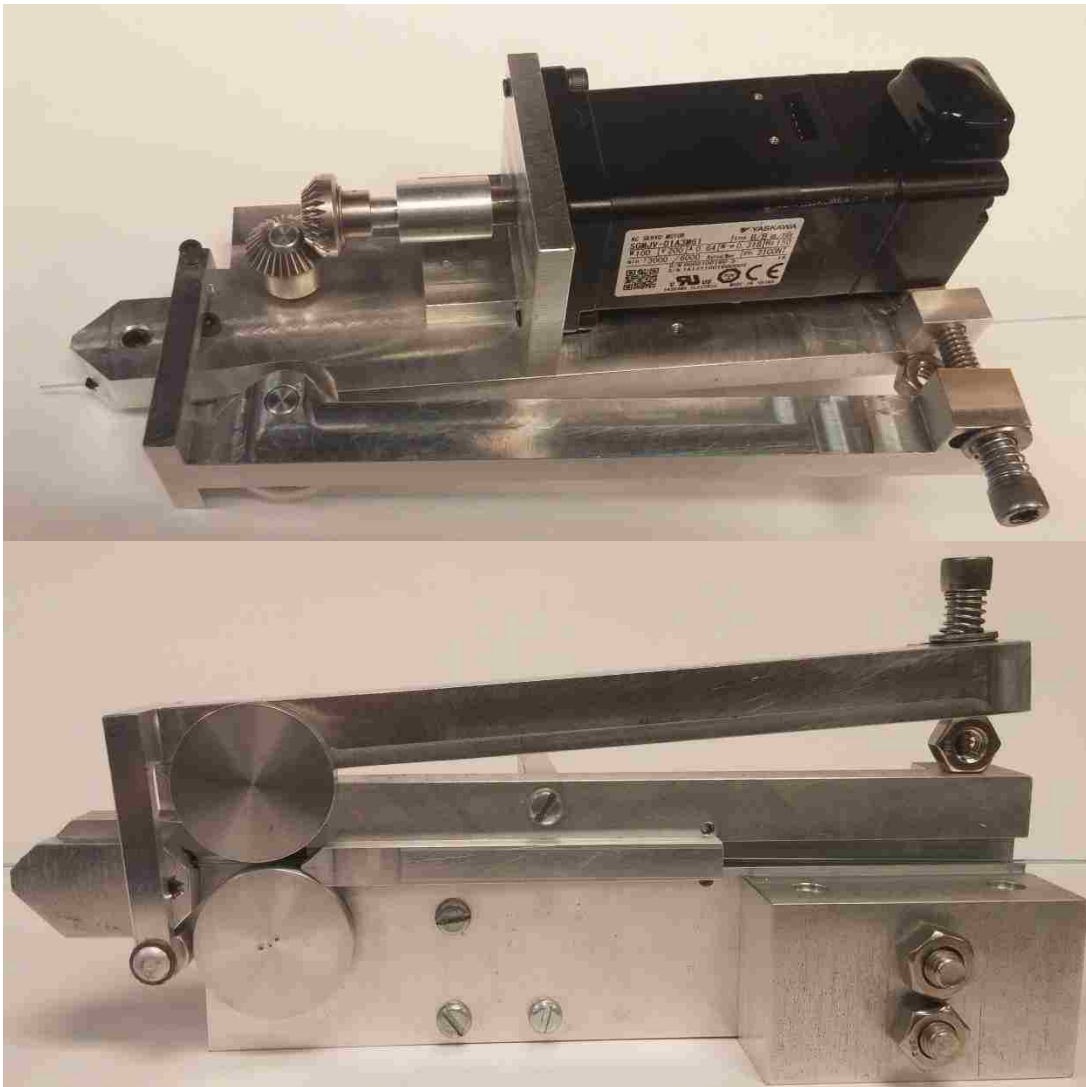


Figure 2.2. New Wire Feeders as Viewed from the Top and Bottom Respectively.

The wire feeder clamp is composed of a compliant spring, and an aluminum plate with a right angle alignment groove cut into it. The plate is attached to the feeding end of

the wire feeder with three bolts and sandwiches the compliant spring between itself and the main body of the wire feeder as seen in Figure. 2.3.

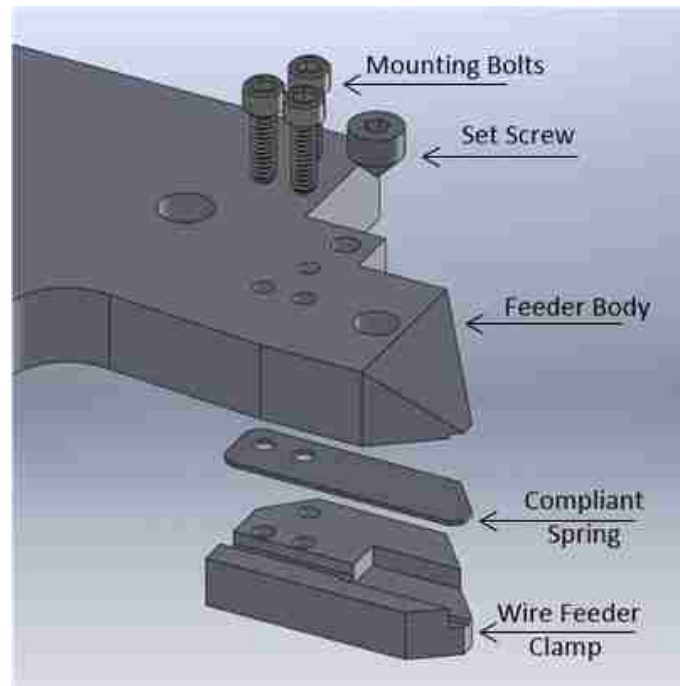


Figure 2.3. An Exploded View of the Wire Feeder Clamping Mechanism.

For coarse adjustments, the aluminum plate, or “wire feeder clamp” was made to be easily detachable. Two wire feeder clamps have been made to address two ranges of diameters, 2 to 0.75 mm, and 0.75 to 0.125mm. By changing the wire feeder clamp and the wire guide, a “T” shaped hollow aluminum piece that supports the wires before they enter the wheels, a wide range of filaments can be fed. A picture of the wire guide is shown in Figure 2.4., and the feeder clamp groove depth, and wire guide diameter for the common range of wire diameters is given in Table 2.1.

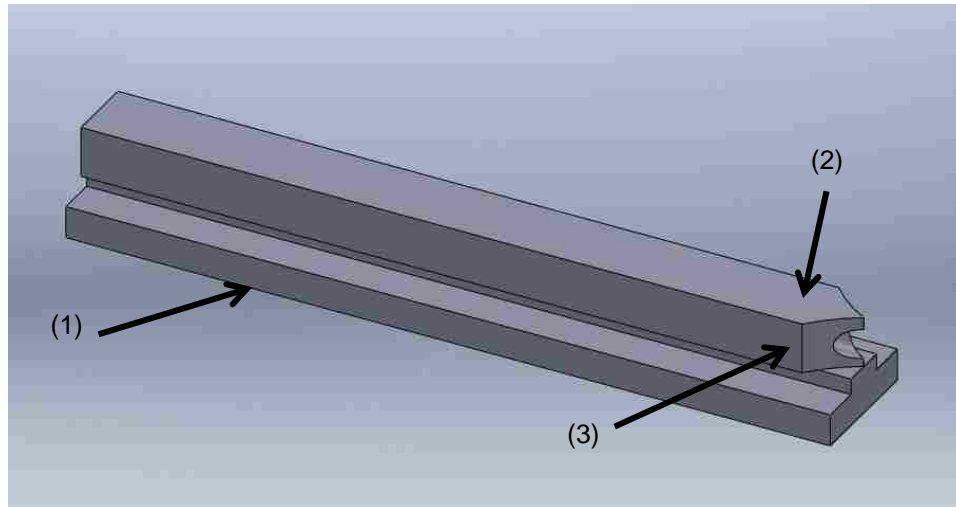


Figure 2.4. Isometric View of the Wire Guide. (1) the flanges that allows the wire guide to fit inside the milled key slot in the body of the wire feeder. (2) the radius of curvature of the bevel matches that of the feeder wheels allowing the wire guide to nearly butt up against them. (3) the channel which the wire passes through before being fed into the wheels.

Table 2.1. The dimensions of the interchangeable parts in the wire feeder needed to feed different diameter wires.

Wire Diameter 0.75-2mm	
Feeder Clamp Groove Depth	0.5 mm
Wire Guide Diameter	3 mm
Wire Diameter 0.125-0.75mm	
Feeder Clamp Groove Depth	0.125 mm
Wire Guide Diameter	1 mm

The wire guide and wire feeder clamp are able to handle a wide variety of wire diameters because both the compliant spring, in the front of the feeder, and the tensioning spring in the back of the feeder are adjustable. The compliant spring is adjusted by

tightening and loosening a set screw, and the tensioning spring is adjusted by tightening and loosening a $\frac{1}{4}$ x 20 bolt.

The new servo motors, Yaskawa (SGMJV-01A3M61), were chosen for their high resolution and due to budgetary constraints. The Yaskawa motors were much larger than the motors used in the prototype wire feeders. Due to their large size they were not able to directly drive the wire feeders without blocking the CO₂ laser's path. To address this, the wire feeder's size was scaled up, and the motors were rotated 90°. Anti-backlash bevel gears were used to translate the torque. The resulting optical path remained unobstructed as shown in Figure 2.5. In order to align them, the feeders were attached to a Thor labs (QRP02) rotational stage and a Newport (DS25-Z) stage so that the precise angle of rotation could be measured and the tips of the wire feeders can be aligned precisely.

2.1.2. Motion Stages and Substrate Heater. The build platform is moved in three dimensional space via Aerotech Stages. The X and Y stages are ANT130-160XY direct drive stages with a resolution of 10nm and a repeatability of 75nm. The stages have a total travel length of 160mm, and a maximum speed of 350mm/s and a maximum acceleration of 10m/s². The maximum continuous current for the stages is 2.94Apk. The Z stage, an ATS100-150, motor driven, ball screw stage, has a repeatability of $\pm 0.7\mu\text{m}$ and a resolution of 0.5 μm , it has a resolution of 10nm and the maximum continuous current for the Z stage is also 2.94Apk. The stage has a total travel length of 150mm, and a maximum velocity of 100mm/s. The Z stage also has a fail-safe brake. The stages are shown in Figure 2.6.

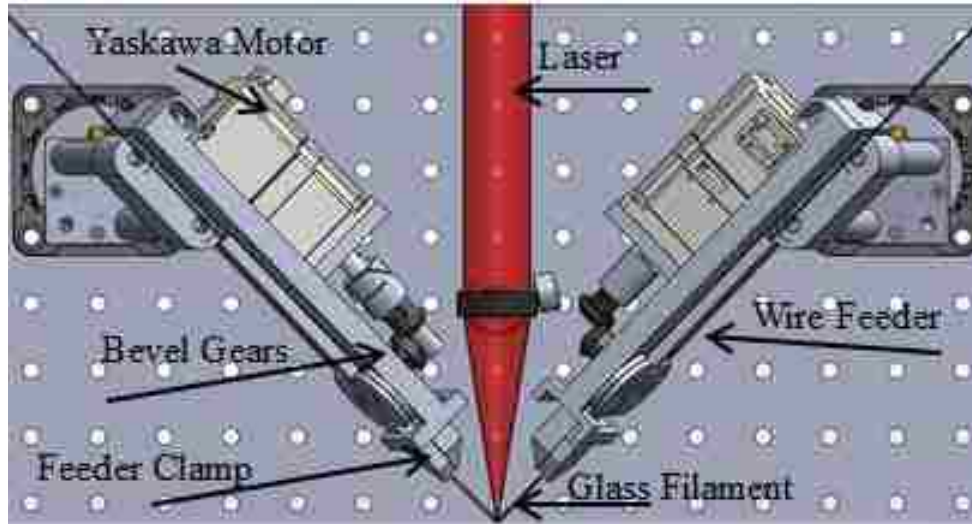


Figure 2.5. The Mounted Wire Feeders and the Unobstructed Optical path of the CO₂ Laser.

The X and Y stages use linear encoders, and have 5 volt normally open limit switches customized by Aerotech. They also have a zeroing “Z signal” at the center of the stage. The Z stage uses a rotary encoder that is converted to a linear measurement inside of the Aerotech amplifiers. The Z stage also has 5 volt normally open limit switches, but as the encoder is a circular encoder, the zeroing “Z signal” of the encoder occurs every revolution of the motor.

The build platform is located on top of a Ceramic Fiber Heater (Watlow VF605A06S) heater, controlled via a Watlow EZ-ZONE PM Express Controller (PM6C1CA-AAAABAA). The temperature of the heater is measured with an 8 gauge type k thermocouple, (Watlow 1409-18). A steel build platform is attached to the top of the heater as glass tends to wet to ceramics. The heater is surrounded by insulation and a radiation shield made of reflective sheet metal to keep the stages from heating. The heater is connected to the stage using four Alumina Silicate Ceramic rods (McMaster-Carr

8479K21) with a 0.25in diameter and 3in length. These ceramic rods in turn are connected to a custom made “L” bracket which connects directly to the stages. The heater is capable of reaching temperatures of up to 700°C, near the annealing temperatures of most glasses. The build platform is shown in Figure 2.7.



Figure 2.6. Aerotech Stages used in the Glass AM Process with the Substrate heater attached.

2.2. OPTICAL SYSTEMS

The optical systems consists of two lasers, a 125 Watt CO₂ (Synrad Evolution 125, $\lambda_0= 10.6 \mu\text{m}$) laser, and a 4.5 mW He-Ne (ThorLabs CPS635F, $\lambda_0=635\text{nm}$) laser,

an NM Laser (LS055S3W8-C2) shutter, an optical lens train, a thermopile power meter (Ophir 10A –V1.1), and An OceanOptics USB-4000 fiber-coupled spectrometer. The lasers and the shutter are water cooled with a Thermo NESLAB M75 Merlin Series chiller. A diagram describing the optical setup is shown in Figure 2.8.



Figure 2.7. The Substrate Heater with a Soda-Lime Glass Slide Bolted Into Place on the Build Platform.

The lasers in the system serve two distinct purposes, the first laser, the CO₂ Laser, provides the energy to generate and maintain the melt pool as most glasses are opaque to the long-wave infrared electromagnetic spectrum. The CO₂ laser has been shown to melt soda-lime [29, 30], borosilicate, fused quartz [31, 32], flint glass, colored art glass, and even alumina . The build platform is placed at the focus of the laser making the Full

Width Half Maximum (FWHM) diameter of the laser beam at the build platform 200 μ m. The power of the CO₂ laser beam is adjusted by hand in an open loop method via a Synrad UC-2000 laser controller. The He-Ne laser is combined with the CO₂ laser and serves as a laser alignment tool, and safety mechanism. As humans cannot see the wavelength of 10.6 μ m, the He-Ne laser is used for alignment by providing a visible representation of the CO₂ lasers. The laser shutter, an NM Laser shutter (LS055S3W8-C2), has an aperture diameter of 12mm, and is used to disrupt the CO₂ laser beam. It has a maximum repetition rate of 5 Hz, and is controlled via a modified G-Code. In order to keep the laser as stable as possible, most processes use the laser at a constant power level, while the shutter turns off and on to start and stop the process. The shutter is hooked up to the emergency stop and initialization Programmable Logic Control (PLC), so that if the emergency stop sequence is triggered the laser beam will be interrupted. The shutter is also water cooled to ensure that it does not over heat when it interrupts the laser.

There are several lenses and mirrors that are used by the Glass AM process. These lenses serve many purposes, but can generally be described as doing three things: combining the CO₂ and He-Ne lasers, diverting 1% of the CO₂ laser beam to the thermopile power meter, and moving the CO₂ and He-Ne laser beams so that they are focused at the build platform.

The Ophir 10A-V1.1 power meter is a thermopile power sensor capable of reading powers between 20mW and 10 Watts. As it is a thermopile sensor it has a relatively slow rise time of 0.8 seconds. The power meter is used to get an in situ reading of the CO₂ lasers output power. Since it can only handle small power ranges, between

20mW and 10 W, 1% of the laser power is diverted from the process and sent to the power meter. The power meter is controlled via an Ophir Nova II power meter.

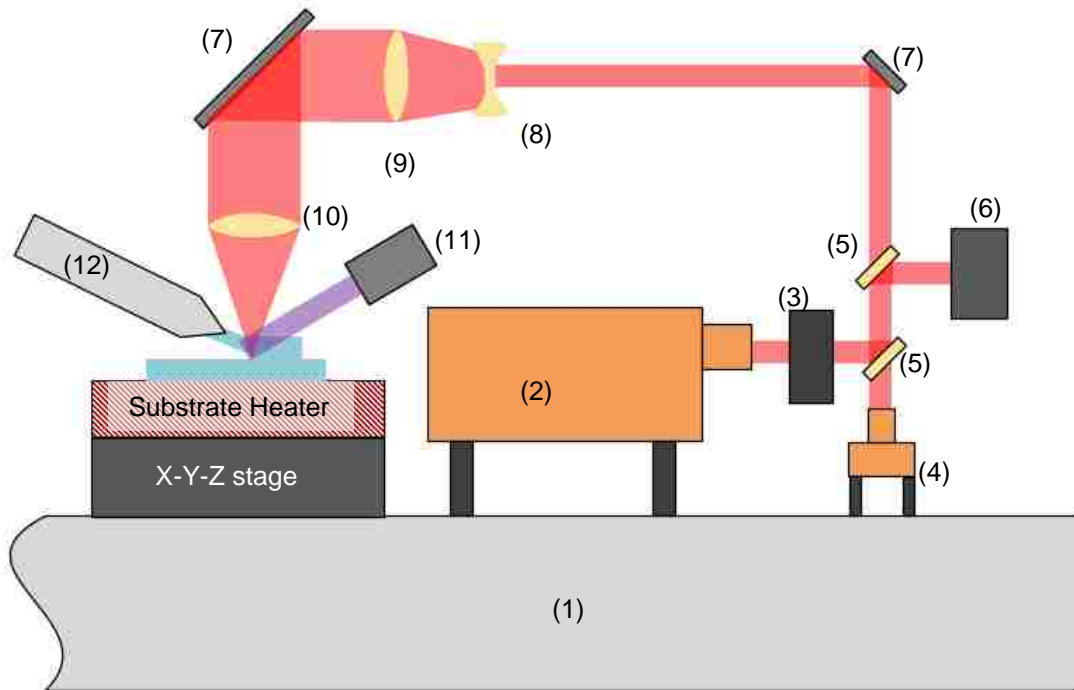


Figure 2.8. Optical Systems Diagram. (1) Vibration Isolation Table. (2) CO₂ Laser. (3) Water Cooled Shutter. (4) He-Ne Laser. (5) Beam Splitters. (6) Power Meter. (7) Mirrors. (8) Beam Expander. (9) Collimator. (10) Focuser. (11) Spectrometer. (12) Wire Feeder.

The OceanOptics USB-4000 fiber-coupled spectrometer is used to observe the melt pool of the process. The spectrometer is mounted 5cm from the melt pool, and resolves the visible and near infrared emissions (200-850nm). It has a variable integration time between 3.8ms to 10 seconds. It is expected that the spectral data of the melt pool will add another source of feedback for a process control as the magnitude of the spectral emission is directly related to the temperature of the melt pool. It has also been observed

that bubble formation in soda-lime glass is accompanied with large spikes in the spectral emissions at unique wavelengths, as shown in Figure 2.9. It is hypothesized that bubble formation may be interrupted by adjusting the laser power when the magnitude of these peaks reaches a critical point [34].

The optical system is also comprised of a water cooling loop. This loop cools the CO₂ laser, and the shutter. This loop itself is cooled by a Thermo NESLAB M75 Merlin Series chiller. The chiller keeps the water in the cooling loop at 20_C ±0.1°C. The Merlin M75 water cooler is able to cool expel 7356 BTU/hr.

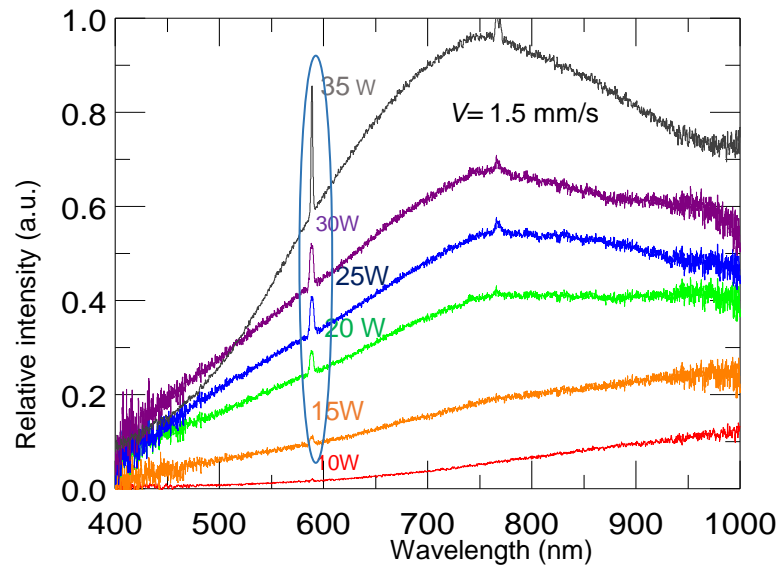


Figure 2.9. The Spectral Emission of the Glass AM System at Various Laser Powers, with a Constant Scan Speed. The Peak at 589nm is Only Found When Bubbles Are Generated.

2.3. ELECTRICAL SYSTEMS

The Glass AM process uses control algorithms and other software to monitor and control the manufacturing of parts. This software requires a complex array of electronics to govern the system. These electronics include a standard Personal Computer (PC), a LabVIEW PXIE Real Time machine, three Aerotech Soloist (HPE 10-IO-MXH), and two Yaskawa Sigma V SGD V MetroLink-III amplifiers, six noise filters, a relay, 5 magnetic disconnects, a Direct Logic 5 D0-05DR-D Programmable Logic Controller (PLC), three emergency stop buttons, three fans, a level step converter, breakers, and five optical isolators, all of which is contained in a 42x36x16 inch electrical cabinet (Saginaw SCE-42H3516LP) , and mounted on a steel panel (Saginaw SCE-42P36). The electrical cabinet is cooled by three Orion fans, (0A109AP-11-2TB). The cabinet is shown in Figure 2.10. and the wiring diagram for the system is shown in Figure 2.11.

Three separate computers control the Glass AM process. The first computer, the Direct Logic PLC, monitors the emergency stop buttons of the Glass AM process, and actuates the relay and magnetic disconnects should any of the emergency stop buttons be pressed. The PLC also handles the initial startup sequence, staggering the start of each of the magnetic disconnects and relays in order to limit the amount of inrush current the entire system draws, as the system is powered solely off of 120 volt, 15 amp A/C power source. The other two computers used are a standard PC, desktop machine running Windows 7, and a LabVIEW Real Time PXIE-1082 system. This system was selected due to its ability to compute complex control signals and manage all of the data acquisition through its vast array of inputs and outputs at over 10 kilohertz. The LabVIEW Real Time chassis does all of the actual computations that affect the Glass AM

system, but the PC contains the user interface that allows one to interact with the Real Time Machine. The PXIE-1082 chassis has eight total expansion slots with a 7 GB/s system bandwidth. The glass AM process only uses three of the eight total slots. The first slot is the controller, an NI PXIe-8135, with a 2.3 GHz quad-core Intel i7 and 4GB of DDR3 Ram. This module is the “brains” of the NI system and, therefore, the glass AM process.

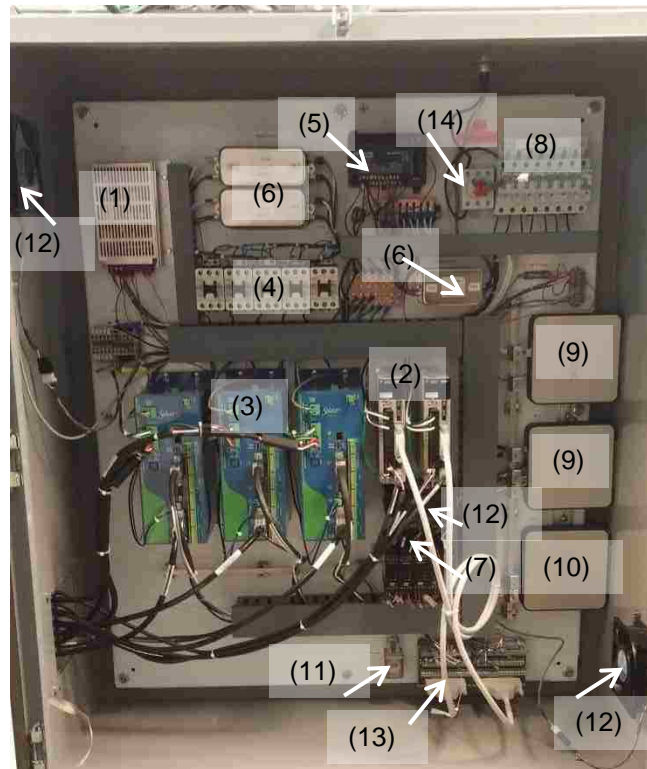


Figure 2.10. Glass AM Electrical Cabinet. (1) Power Supply. (2) Yaskawa Amplifiers. (3) Aerotech Amplifiers. (4) Magnetic Disconnects (5) PLC. (6). Noise Filters. (7) Optical Isolators. (8) Breakers. (9) PXIe 6612 Pinout Board. (10) PXIe 6673 Pinout Board. (11) Shutter Relay. (12) Fans. (13) Yaskawa Pin Outs. (14) Main Disconnect.

The second slot is used for an NI PXIe-6356. The NI PXIe-6356 is a DAQ board capable of measuring eight 16-bit analog inputs, two 16-bit analogue outputs, 24 digital I/O points, and has four 32-bit counter timers. This board is currently unused, but will be used in future expansion.

The third slot of the PXIe-1082 is for the PXIe-6612. The PXIe-6612 specializes in encoder signals and pulse width modulation. The PXIe-6612, sometimes called a “Counter/Timer board”, has eight 32-bit counters and 40 digital I/O points. This board is exclusively used to count the number of pulses that are delivered to it from the encoders on the stages and wire feeders, but it does also function as a second digital communication board for the proprietary amplifiers. The PXIe have a maximum sampling rate of 80 Mhz on the counters. The fourth slot is a second PXIe-6612. This board is used mainly for digital communication with the proprietary amplifiers, and the shutter. This includes the Aerotech Soloist HPE 10-IO-MXH modified for torque control for the Aerotech Stages and the Yaskawa Sigma V amplifiers for the wire feeder motors.

The final board, the PXI-6733, is a high speed analog output board. This board is capable of maintaining eight 12-bit analog outputs. It is through this board that the analogue controller command signals are relayed to the proprietary amplifiers and the stages and wire feeders are controlled. The electrical signal wiring is shown in Figure 2.12.

The Aerotech Soloist amplifiers have two separate voltage supplies, a motor supply and a control supply. Both power sources pass through a Schafner (FN2070-10-06) filter. The motor supply voltage passes through a Fuji Magnetic Disconnect (SC-E03G-24VDC) which is controlled by the PLC.

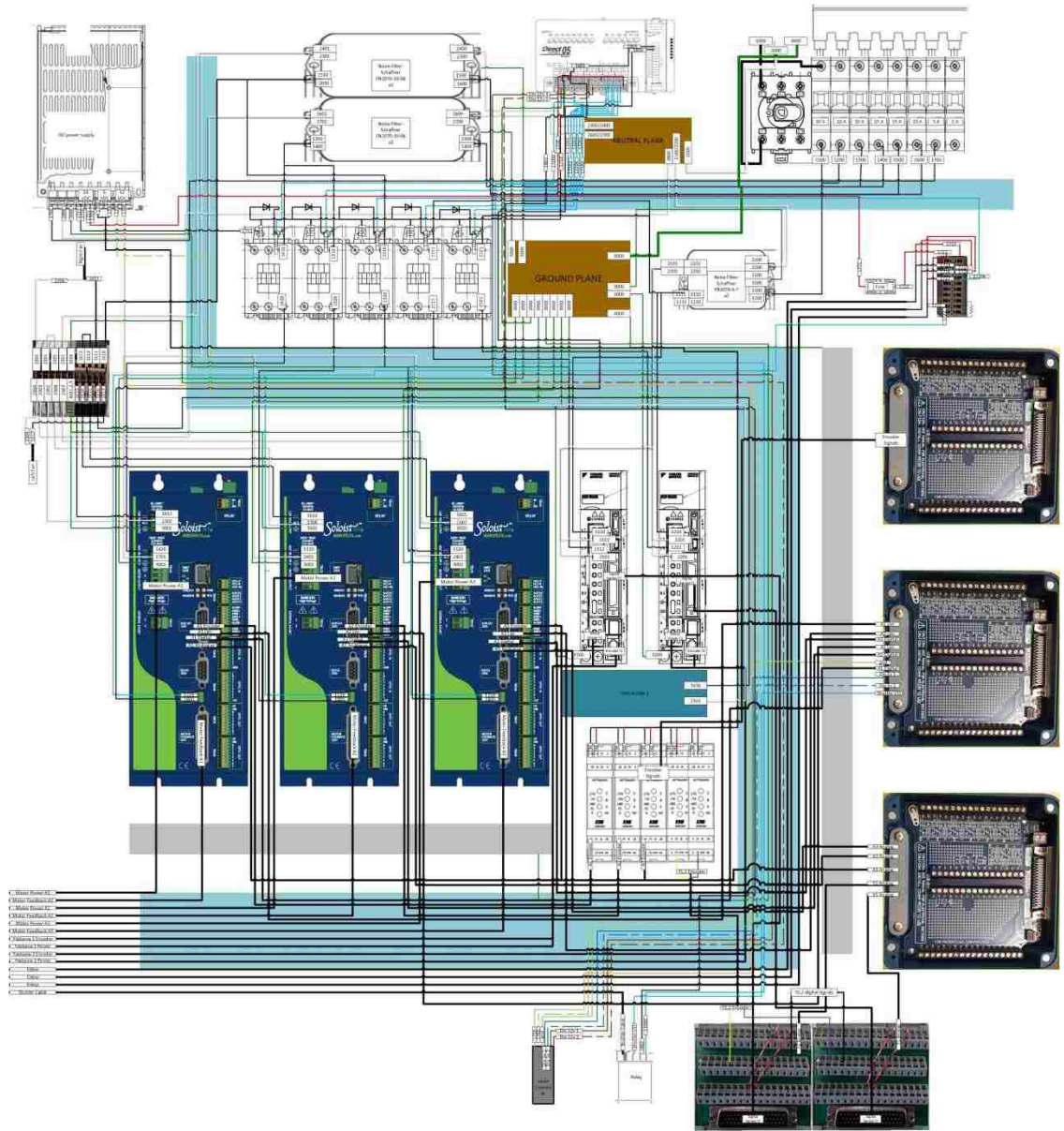


Figure 2.11. Glass AM Electrical Cabinet Wiring Schematic.

The amplifier communicates to the LabVIEW system using a custom made Auxiliary cable. This cable contains the encoder signals, which pass through a BEI optical isolator (EM-DRI-IC-5-TB-28V/V), the enable signal, the limit switch signals, the fault signal, and the control signal voltage. The Amplifiers have an encoder resolution of

100,000 pulses per mm. This signal is down sampled by a quarter by the amplifier and sent to the LabVIEW system.

The Yaskawa amplifiers (SGDV Mechatrolink-III) also have two separate voltage supplies, a motor supply and a control supply. Both sources pass through a Schaffner line filter (FN2070-6-07). The motor supply voltage passes through a Fuji Magnetic Disconnect, and just like the Aerotech amplifiers, the magnetic disconnects are controlled by the PLC. The amplifier communicates to the LabVIEW system using a proprietary pin out system. The encoder signals pass through the same type of BEI optical isolators as the Aerotech amplifiers before reaching the NI system. The enable signal, fault signal, the clear fault signal, and the control signal voltage are also passed to the LabVIEW system through this system.

The amplifiers have a variable encoder resolution between 16 and 262144 pulses per revolution. For the glass AM application this number is set to 131072 pulses per revolution so that the maximum speed is 12.5 revolutions per second, or 1178 meters per second.

The magnetic disconnects and relay are powered by the DC power supply, it takes both the PLC and the DC power supply to work in order for the motor power to reach the amplifiers, and the 5 volt actuating signal to open the shutter. An emergency stop can be triggered by interrupting the normally closed 24 volts emergency stop signal, or by outputting a 5 volt signal from the LabVIEW system into the custom designed level stepper, which interrupts the normally closed 12 volt LabVIEW emergency stop signal. An electrical diagram of the level stepper is found in Appendix A, along with a complete list of signals.

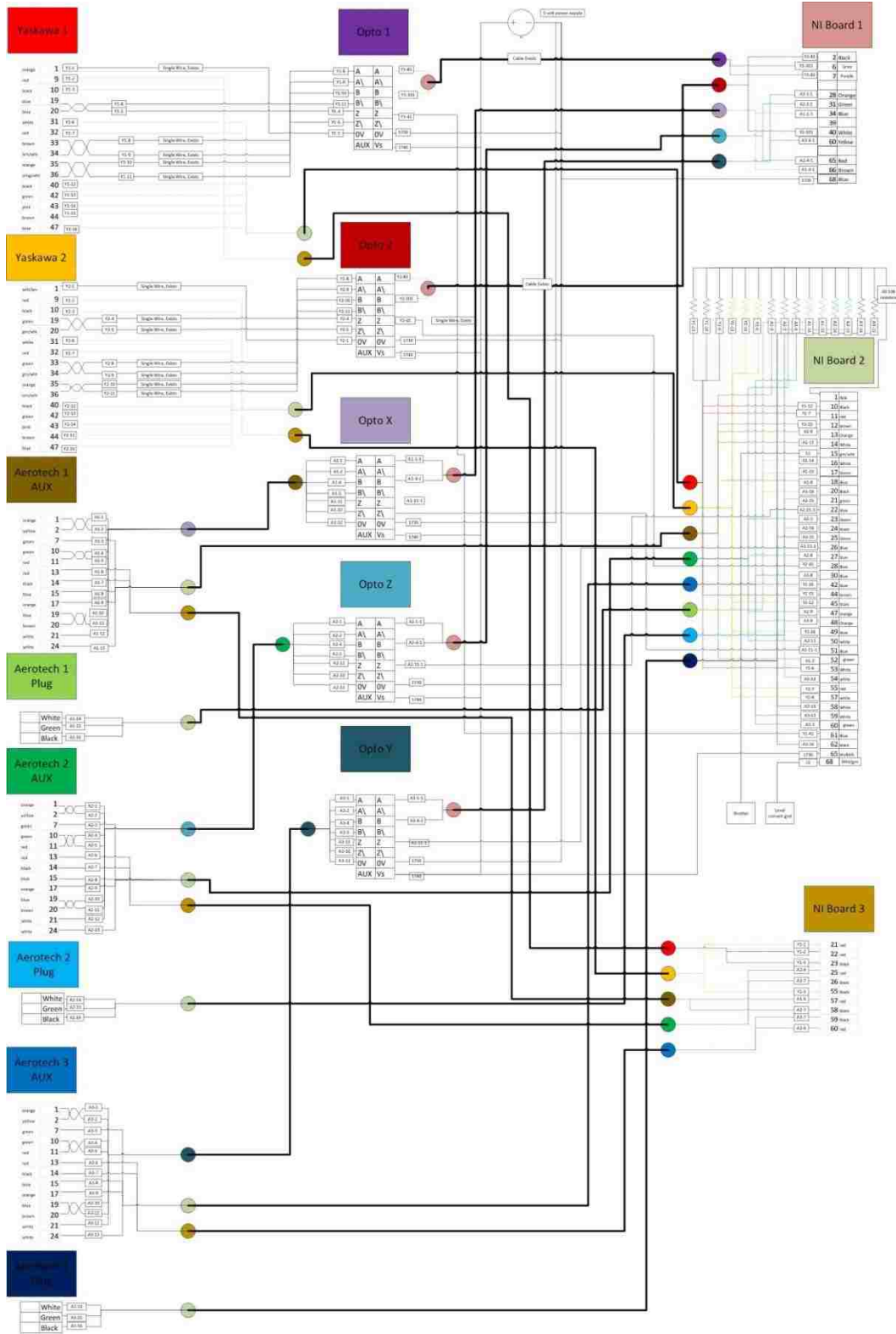


Figure 2.12. Glass AM Electrical Signal Wiring.

2.4. SOFTWARE SYSTEMS

The goal for the glass AM process is to be able to create AM parts directly from a three dimensional CAD drawing. In order to do this, many different programs must all interface with each other. The way the different computers and programs interact is outlined in Figure. 2.11. The first step in creating a Glass AM part is to create a 3D CAD model of the part that is to be created using a 3D CAD software. After the part has been designed, the part is loaded into Slic3r. Slic3r is an open source program which takes 3D parts and turns them into G-Code. This G-code will have to be customized as the Glass AM process is entirely new. Instead of starting a machine tool and setting its speed, the laser's shutter will have to be opened and the laser's power level will have to be set. The speed of the wire feeders must also be set using G-Code.

The G-code is then deconstructed by a G-code parser. This parser exists on the NI Real Time machine in a non-deterministic loop which cycles every 0.02 seconds. Once this G-Code has been parsed out the interpreter sends the relevant information: scan speed, feed rate, laser power, etc. to the deterministic control loop, which cycles at 10 kHz.

The interpreted data from the G-code is separated and the velocity and acceleration vectors and magnitudes are calculated. The designated path is then generated point by point by a linear interpolator with constant acceleration. This leads to a Linear Segment Polynomial Blend (LSPB) velocity profile. Depending on the G-Code command, a straight line is generated, or a circular path is generated. The calculations behind the velocity and acceleration vectors, and the point-by-point path generation, are included in Appendix B.

This point-by-point reference signal is passed to the PI and PID controllers for the wire feeders and motion stages. These control loops generate a command voltage which is relayed to the various proprietary amplifiers that control the stages and servo motors. The encoders connected to the motors and stages, in turn, send back their position in encoder counts.

The NI Real Time system also has a safety subroutine which monitors the speed, current, position, and error of the system. If an error is triggered by this subroutine, the shutter is closed, and the current sent to the stages and wire feeders is set to 0 amps. The motors are disabled and the Z stage's brake is engaged. More detail about the types of errors and calculations of errors are found in Appendix B.

At the highest level a Direct Logic 5 D0-05DR-D PLC controls the startup of the glass additive manufacturing system, and monitors the system for an emergency stop. At the startup of the system the PLC staggers the amplifiers start up by half a second to make sure the inrush current does not trip any breakers. Once the startup sequence is complete, the PLC monitors the Emergency Stop buttons, the DC power supply, and the Level Step Converter. If any one of these systems should fail, the PLC disconnects power to the amplifier's motor circuit by shutting off the magnetic disconnect.

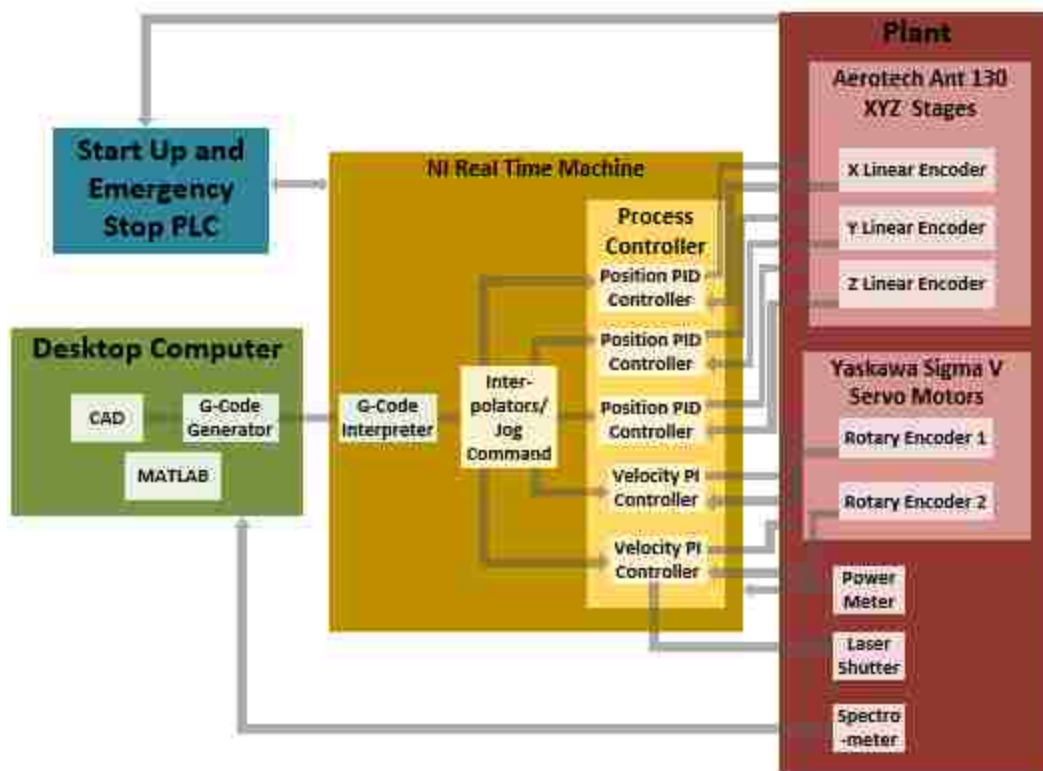


Figure 2.13. Software Systems Hierarchy Block Diagram.

3. SYSTEM CONTROL

3.1. WIRE FEEDER CONTROLLERS

An attempt was made to control the wire feeders with a PID controller; however, after trying to tune the controller to a step velocity input of 0.5 mm/s, it was found that the system was unstable. Upon inspection, the motors were found to have large nonlinear cogging forces which tended force the system to go unstable. To verify this, a control voltage of 0.19 volts with a 100Hz, 0.01 volt amplitude sine wave was used to excite the system. For a linear motor one would expect that a constant voltage would elicit a constant velocity once the motor reached steady state, however what was observed was a highly variable velocity profile, shown in Figure 3.1.

The velocity changes drastically as the motor makes a full revolution. This quick change in velocity combined with the noise sensitivity to an Euler backwards different method derivative, forced the motors to go unstable. The solution to this was to tune the controllers using a weak PI controller. The PI controller is able to keep the velocity of the Yaskawa motors constant within ± 1 mm/s after the transient response dies out. Both of the motors were found to respond similarly, and were both tuned to

$$C(s) = 0.01 + \frac{1.7}{s} \quad (1)$$

This controller is able to keep the velocity centered on the reference input as shown in Figure 3.2.

The position plot of the test shown in Figure 3.2 is shown in Figure 3.3. This figure shows that while there is an initial transient response to the reference input, the system reaches a steady state response with a steady state error of about 0.12 mm.

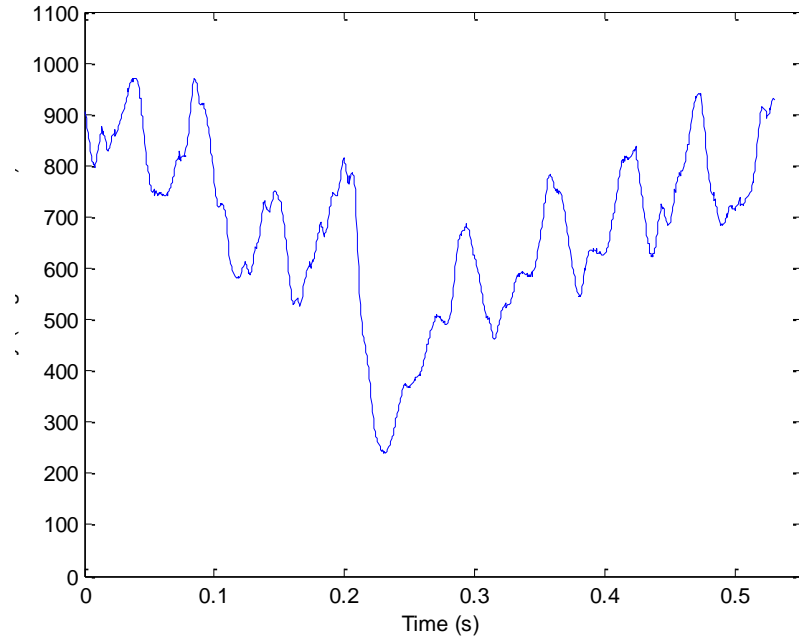


Figure 3.1. Velocity Response of a Single Revolution of a Yaskawa Motor to a Constant Voltage Input with a 100 Hz Dithering Signal.

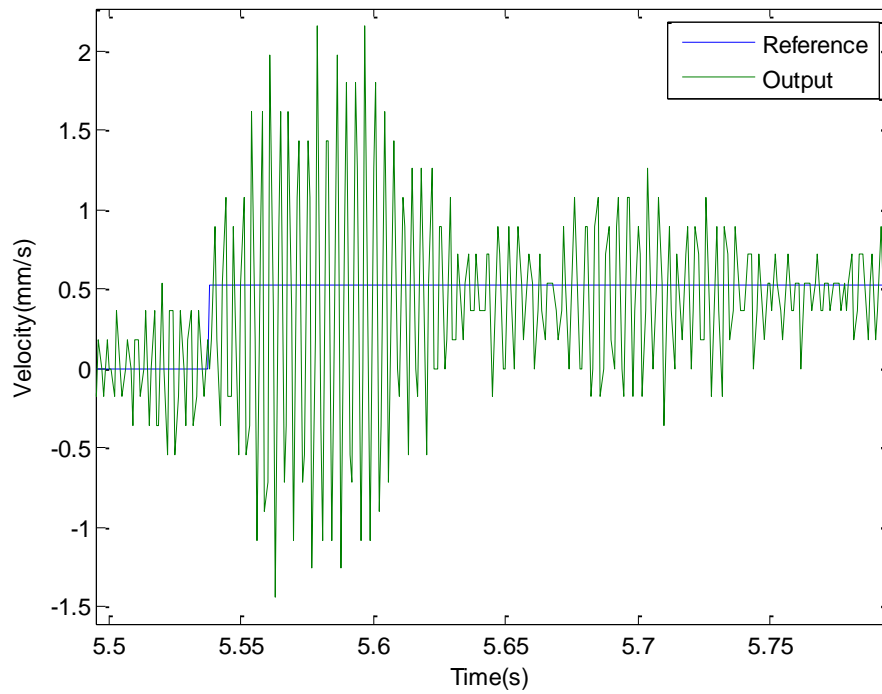


Figure 3.2. Velocity Response of a Wire Feeder Tuned with a PI controller with the gains 0.01 and 1.7 respectively.

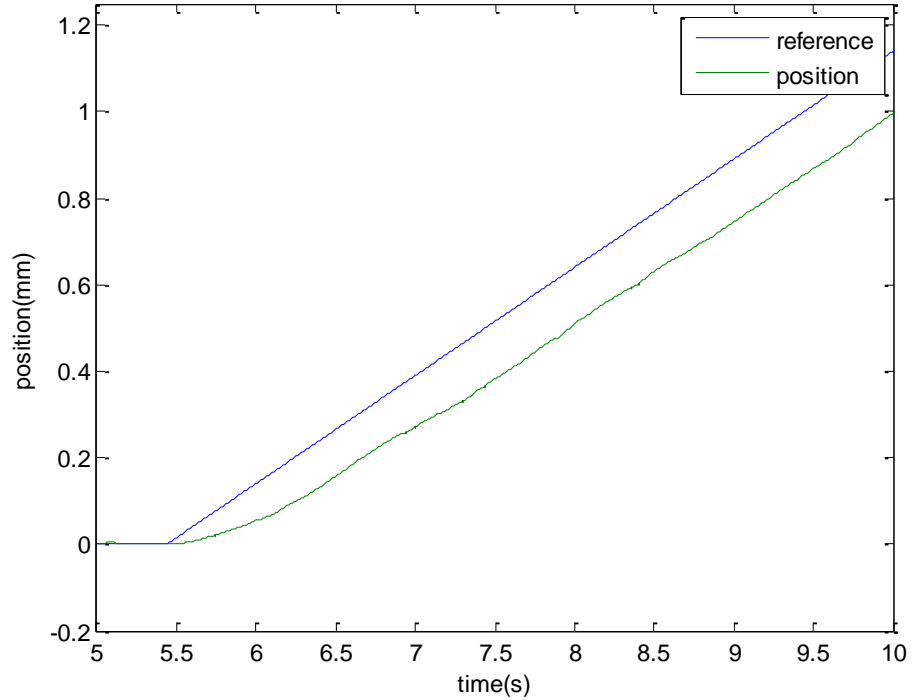


Figure 3.3. Position Plot of the test shown in Figure 3.2.

The time constant of the controlled motor is 454 s^{-1} calculated by finding the first time the response got within 63.2% of the reference value. The transient response dies out after .2 seconds and it has a percent overshoot of 300 %. Due to the large cogging forces and the noise induced by the derivative, settling time has little meaning.

3.2. AEROTECH STAGE CONTROLLERS

A PID controller was created for each of the Aerotech stages. The controllers were tuned by exciting the system with a 0.02mm square wave at a frequency of 0.25 Hz, and a ramp function from -4mm to 4mm at a frequency of 0.5Hz. These signals were chosen as a 0.02mm step would be one of the largest steps the stages would be expected

to handle and the ramp function emulates a constant velocity movement of 4mm/s which is at the high end of velocities that the system is expected to perform at. The controllers were tuned by hand by increasing the proportional gain until the system went unstable. From this point the integral gain was increased until the system started to oscillate. Once the system started to oscillate the derivative gain was increased. This process was repeated until the maximum occurring error was below 0.05mm. The results from the tests are shown for the X stage in Figures 3.4. and 3.5., for the Z stage in Figures 3.6. and 3.7., and the Y stage in Figures 3.8. and 3.9. The percent overshoot, settling time, steady state ramp error, and time constant are discussed in the conclusion. The corresponding controllers are,

$$C_x(s) = 21 + \frac{26}{s} + 0.2s, \quad (2)$$

for the X stage,

$$C_y(s) = 47 + \frac{25}{s} + 0.21s, \quad (3)$$

for the Y stage, and

$$C_z(s) = 58 + \frac{51}{s} + 0.2s, \quad (4)$$

for the Z stage.

The Y stage was found to be more oscillatory than the X stage, as the Y stage aligns with the side of the vibration isolation table which has the smallest moment of inertia; this leads it to be less damped than the X and Z stages. This phenomenon is also observed in Bode plots taken of the stages.

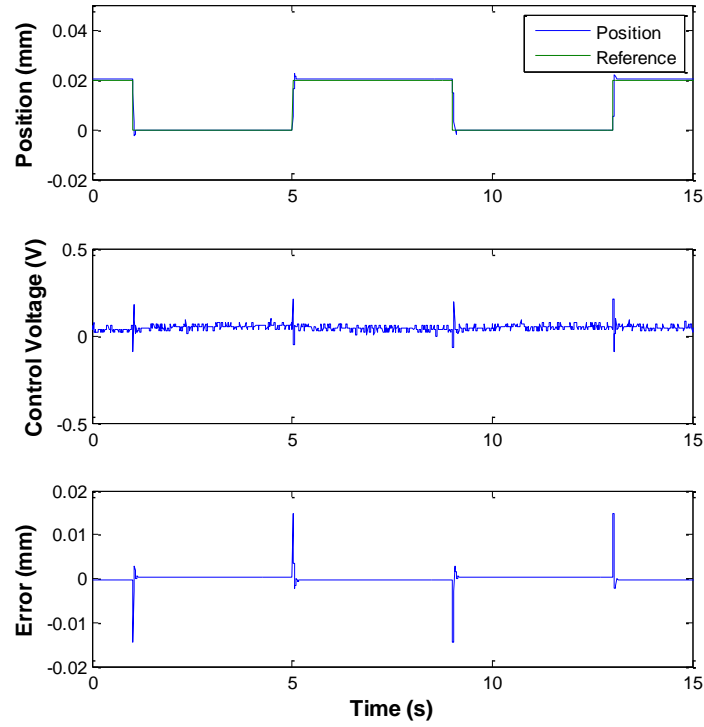


Figure 3.4. X Stage Response to a Square Wave.

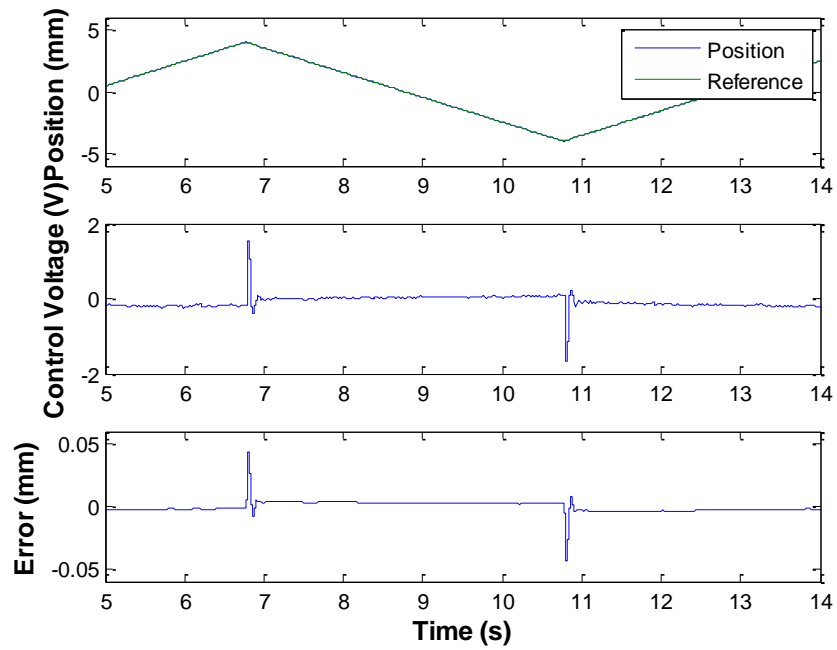


Figure 3.5. X Stage Response to a Ramp Function.

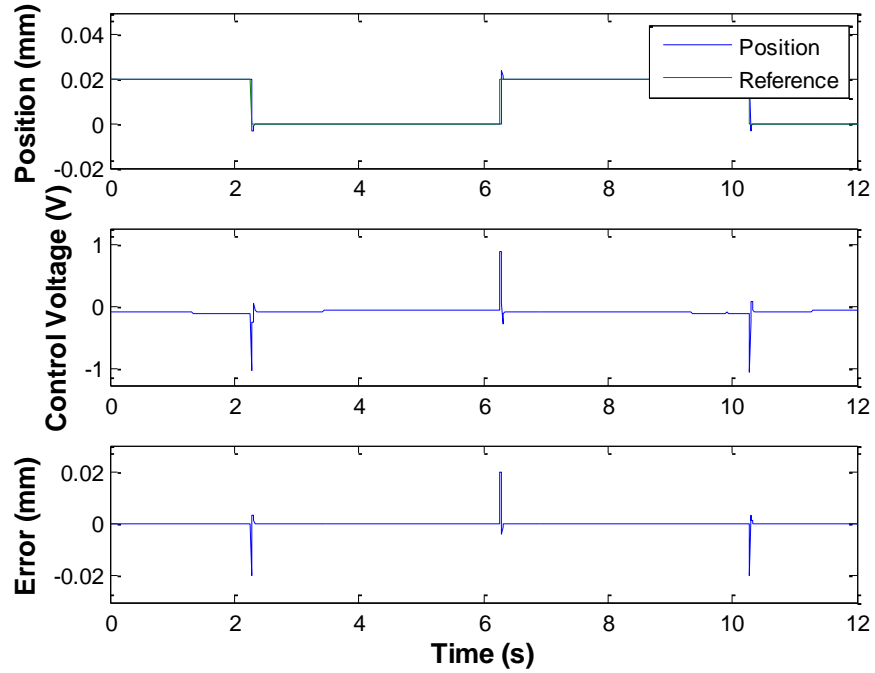


Figure 3.6. Z Stage Response to a Square Wave.

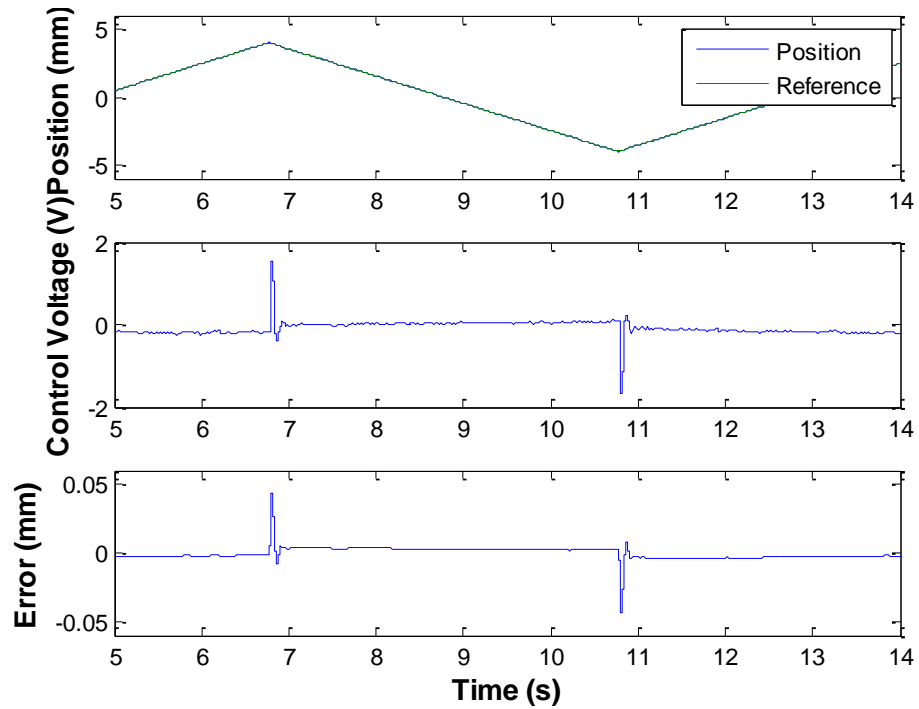


Figure 3.7. Z Stage Response to a Ramp Function.

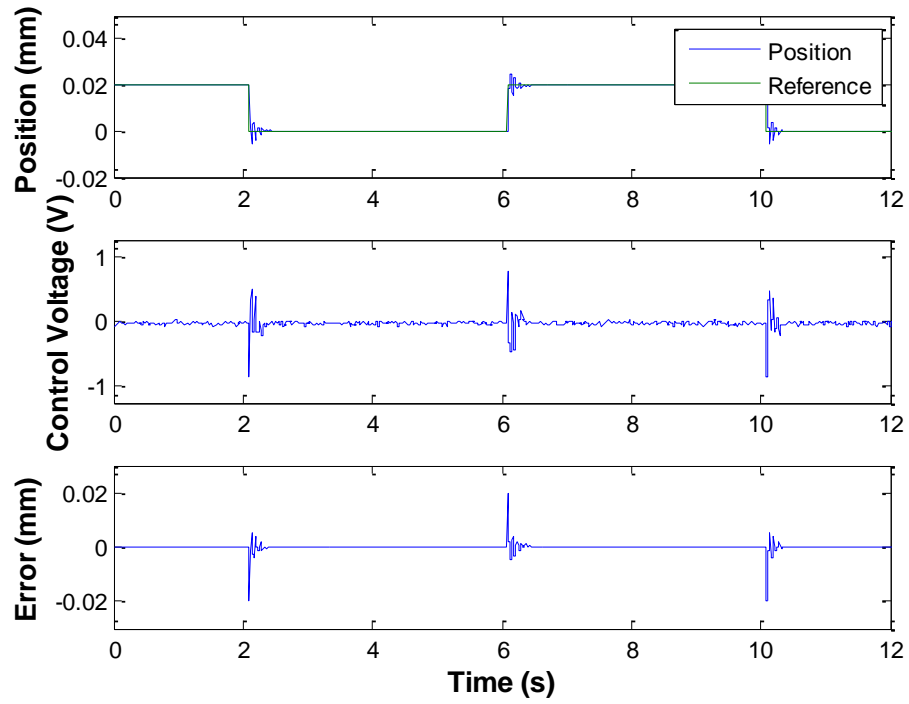


Figure 3.8. Y Stage Response to a Square Wave.

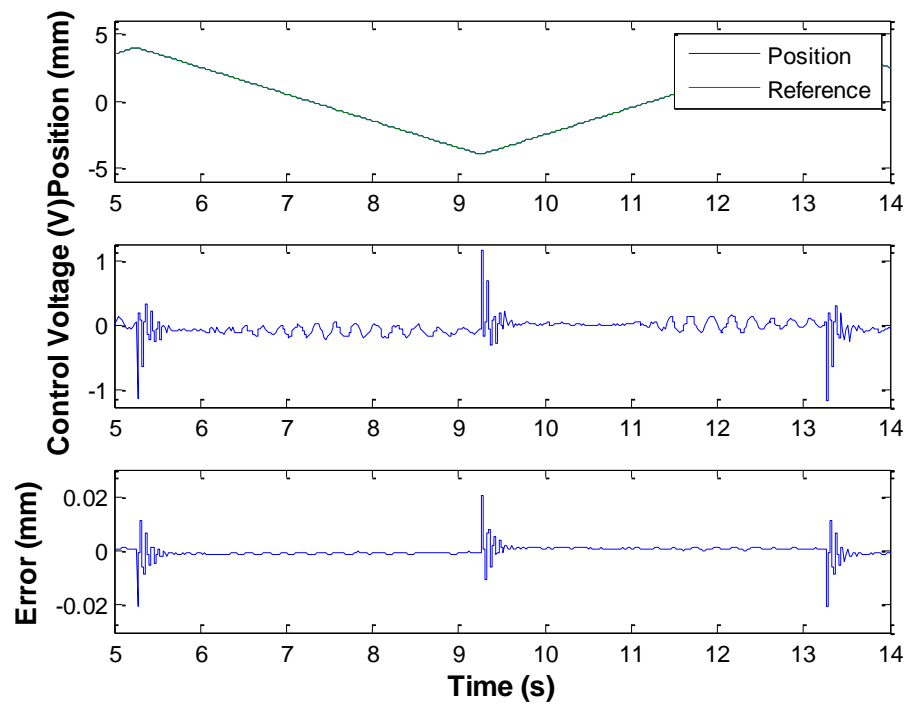


Figure 3.9. Y Stage Response to a Ramp Function.

4. PROCESS MODELING

Glass at high temperatures is purely viscous, while glass at low temperatures is purely elastic in nature. In most case, high temperature glass is a Newtonian fluid except when under large shear stresses. When under large shear stresses glass tends to behave in a shear thinning manner. It is only near the glass transformation range that glass acts in a viscoelastic behavior.

As shown in Figure 4.1., there are several important viscosities related to manufacturing glass. These viscosity points include the melting temperature, where the glass is considered fully liquid, the working point, where most glass manufacturing takes place, the Littleton Softening Point, the viscosity at which glass is able to support its own weight, the annealing point, the point at which internal stresses are “substantially relieved in a few minutes”[35], and the strain point, the temperature where annealing no longer occurs [35] .

Two other temperatures are shown, the Dilatometric softening temperature, T_d , which is defined as “the temperature where the sample reaches a maximum length in a length versus temperature curve during heating of a glass.” [35], and the second temperature the Glass Transformation Temperature, T_g , which “can be determined from measurements of the temperature dependence of either the heat capacity or the thermal expansion coefficient during reheating of a glass.” [35] This temperature occurs at viscosities around $10^{11.3}$ Pa*s [35].

Most manufacturing of glass takes place near the working point, at 10^3 Pa*s. A viscous mass of liquid, called a gob is formed into shapes from the original melt. As the melt pool temperatures of the process have been calculated to be between 1200°C and

1500°C[34] the melt pool is assumed to be completely viscous in nature. Due to the small mass of the melt pool compared to the mass of the filament, and work piece the mass of the melt pool is considered negligible.

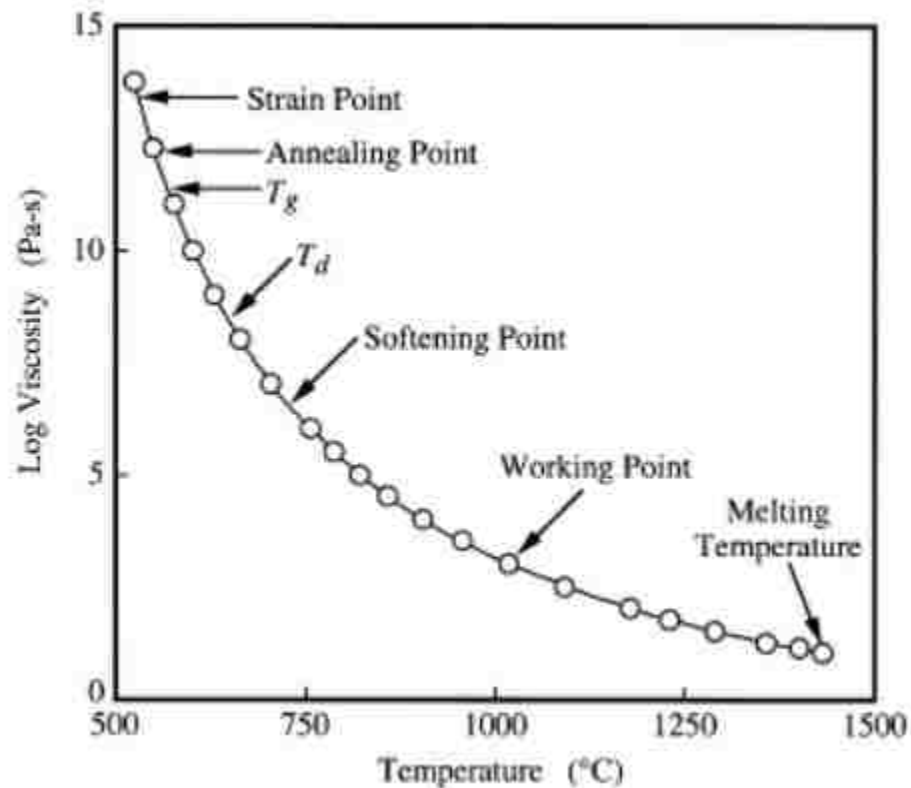


Figure 4.1. Commonly Used Temperatures in Glass Manufacturing for Soda-Lime Glass [35]—Reproduced by permission of The Royal Society of Chemistry.

The Glass Additive Manufacturing (AM) process feeds a glass wire into a melt pool created by a CO₂ laser. This wire is deposited onto a substrate of matching material. The Glass AM process contains four points that are critical to the modeling of the system. The first critical point is the point at which the glass becomes viscous enough to not be

affected by the melt pool dynamics. This point is the solidification front, x_s , and is defined as the point at which the viscosity η , is equal to 1000 Pa-s and the glass is at its working point. The second point of interest is the point at which the wire is deflected to by the viscosity of the melt pool. This point, x_w , is also the point at which the melt pool is centered. The third point of interest is the nominal point of the tip of the wire, x_N , the point at which the glass wire would be if there was no load at its tip. The fourth and final point of interest is the leading edge of the melt pool x_m . The leading edge of the melt pool is dependent upon the mass flow rate, and the viscosity of the melt pool. This process is highly dependent upon the velocity of the substrate, v , and the velocity of the wire feeder, v_w . An illustration of this process is shown in Figure 4.2.

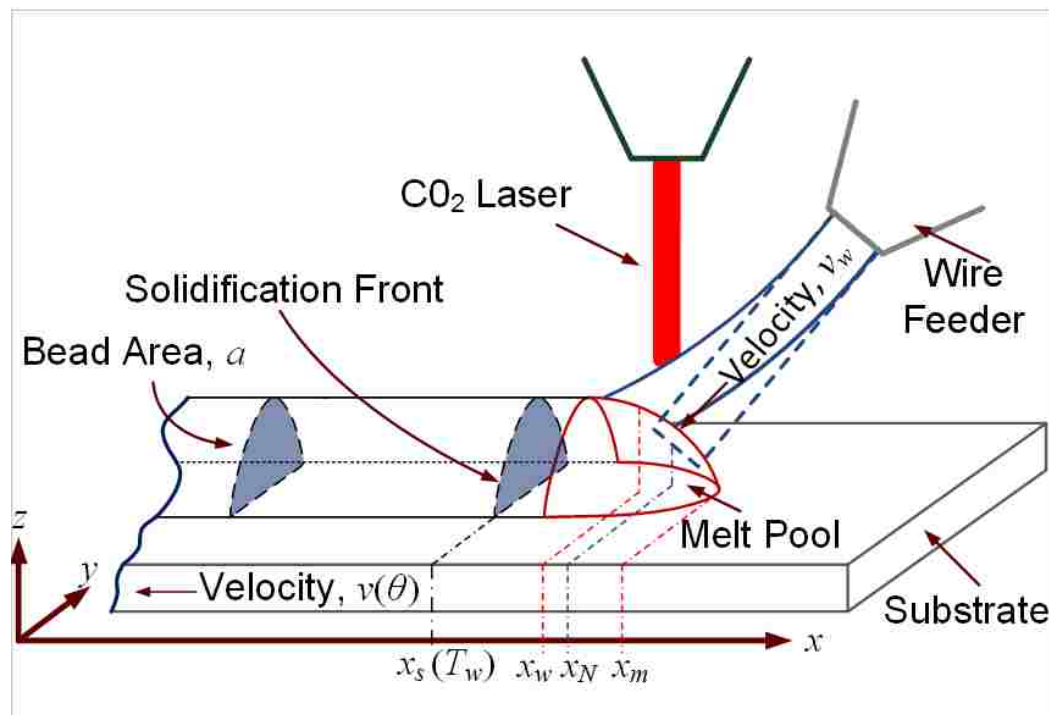


Figure 4.2. Schematic Detailing the Physics of the Glass AM Process.

As glass' viscosity changes drastically with respect to temperature, the actual model of the Glass AM process would need an infinite number of dashpots. As these dashpots are all in series, they can be summed up as an equivalent viscosity, η_{eq} , at a given bulk temperature T_b . Similarly the leading edge of the melt pool can be described as some equivalent viscosity η_m , at some bulk temperature T_m . The bending of the glass wire can be described as a spring with a spring constant K , and the location of the solidification front, x_s , is described as dependent upon the working temperature, T_w . This allows the deposition process to be modeled as a massless spring and damper system shown in Figure 4.3.

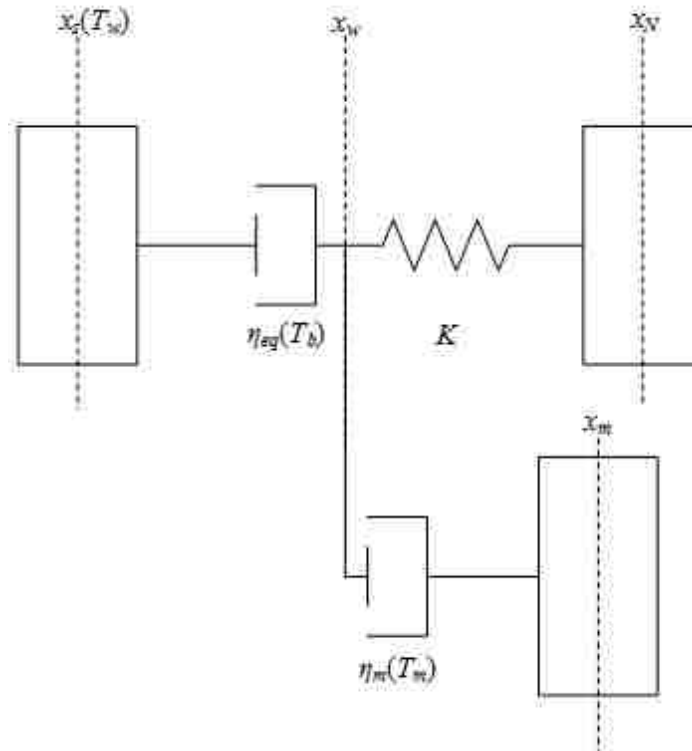


Figure 4.3. Equivalent Massless Spring Damper Model.

The equivalent viscosity is temperature dependent and will need to be discovered through experimentation with different process parameters. The spring constant, K , can be derived analytically from Euler's Beam equation for deflection of a cantilever beam with a force perpendicular to the tip. For a circular cross sectioned beam with an area moment of inertia, I , and a radius, r , such that,

$$I = \frac{\pi r^4}{4} , \quad (5)$$

E is the modulus for the glass wire, and l is the length of the glass wire, the spring constant, K , is calculated as

$$K = \frac{3EI}{l^3} . \quad (6)$$

When the forces are summed around the point x_w the system can be represented as a single differential equation

$$(\dot{x}_w - \dot{x}_m)\eta_m(T_m) + (\dot{x}_w - \dot{x}_s)\eta_{eq}(T_b) = (x_N - x_w)K . \quad (7)$$

Taking the Laplace Transform of (7) with zero initial conditions yields

$$s\eta_m(T_m)(X_w(s) - X_m(s)) + s\eta_{eq}(T_b)(X_w(s) - X_s(s)) = (X_N(s) - X_w(s))K . \quad (8)$$

Solving (4) for the actual position of the glass wire, $X_w(s)$, yields,

$$X_w(s) = \frac{\eta_m(T_m)X_m(s)}{(s(\eta_{eq}(T_b) + \eta_m(T_m)) + K)} + \frac{\eta_{eq}(T_b)X_s(s)}{(s(\eta_{eq}(T_b) + \eta_m(T_m)) + K)} + \frac{KX_N(s)}{(s(\eta_{eq}(T_b) + \eta_m(T_m)) + K)} . \quad (9)$$

Taking the Inverse Laplace Transform of (9),

$$\begin{aligned} \dot{x}_w = & \frac{-K}{(\eta_{eq}(T_b) + \eta_m(T_m))} x_w + \frac{\eta_m(T_m)}{(\eta_{eq}(T_b) + \eta_m(T_m))} \dot{x}_m \\ & + \frac{\eta_{eq}(T_b)}{(\eta_{eq}(T_b) + \eta_m(T_m))} \dot{x}_s + \frac{K}{(\eta_{eq}(T_b) + \eta_m(T_m))} x_N \end{aligned} \quad (10)$$

This means that the position of the glass wire is a first order system with three disturbances: a disturbance from the velocity of the leading edge of the melt pool, the disturbance from the velocity of the solidification front, and the disturbance from nominal position of the wire feeder.

A similar exercise can be done for the melt pool in the Y direction. As shown in Figure 4.4., the Y position of the melt pool is dependent upon three critical points y_m , the edge of the melt pool closest to the wire feeder, y_w , the nominal Y position of the melt pool, and y_M , the edge of the melt pool furthest from the wire feeder.

As the wire is relatively stiff in the feed direction so the spring force along the feed axis is neglected. A free body diagram can be created using only the viscosities of the inner, and outer portions of the melt pool η_m , and η_M , which are dependent upon the bulk temperatures of the melt pool T_m , and T_M , respectively. This diagram is shown in Figure 4.5.

Summing up the forces about the point y_w , yields

$$(\dot{y}_w - \dot{y}_m)\eta_m(T_m) = (\dot{y}_M - \dot{y}_w)\eta_M(T_M) \quad (11)$$

Taking the Laplace Transform and solving (11) for y_w yields a static equation that only changes with respect to temperature. Solving the Laplace equation and taking the inverse Laplace Transform yields

$$y_w = \frac{\eta_m(T_m)}{\eta_m(T_m) + \eta_M(T_M)} y_m + \frac{\eta_M(T_M)}{\eta_m(T_m) + \eta_M(T_M)} y_M \quad (12)$$

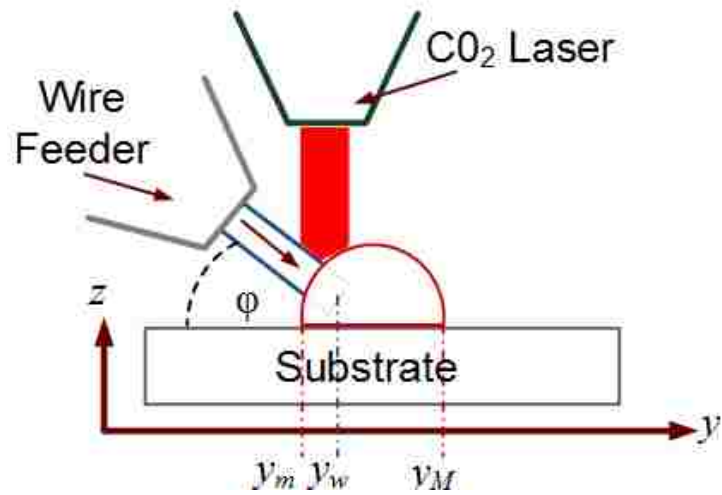


Figure 4.4. Rotated View of the Glass AM Deposition Process.

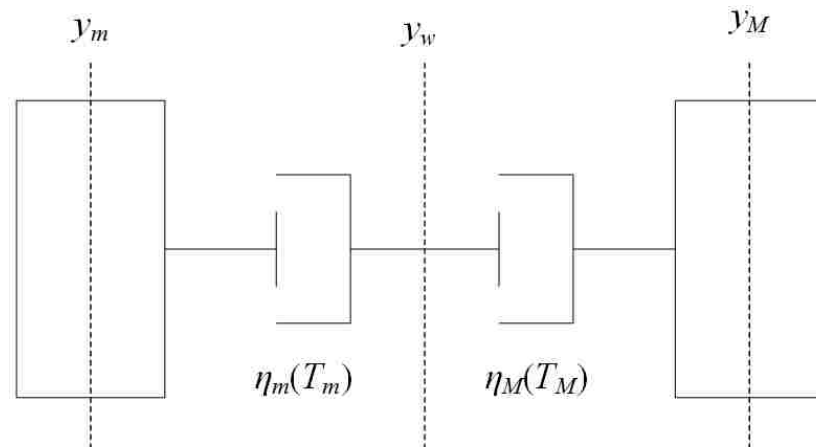


Figure 4.5. Equivalent Massless Spring Damper in the Direction Perpendicular to the Feeding Direction.

5. RESULTS AND ANALYSIS

Of the 10 design goals set out to accomplish by designing an automated Glass AM process, all 10 were met. The first goal was to minimize deflection by designing the wire feeders to get within 10mm of the melt pool. To quantify the bending, the worst case scenario of deflection was calculated. The assumptions for the “worst case” bending scenario are as follows, the dominating force on the wires is the viscous friction in the melt pool. The viscous force can be modeled as a laminar shear of fluid between two plates, the viscous force is calculated given that the maximum scanning velocity used in operation, $u=10\text{mm/s}$, glass is considered liquid at a viscosity, $\mu =1000 \text{ Pa}\cdot\text{s}$ [35], A is one half the surface area of a cylinder with a diameter equal to that of the wire being fed, and the depth of the melt pool 0.5mm. Given this the force, F , can be calculated as

$$F = \mu A \frac{u}{y} . \quad (13)$$

The wire extended from the wire feeder is modeled as cantilever beam where L is the length of the beam, 6cm for the old wire feeder, and 10mm for the new wire feeder, and I is the area moment of inertia where r is the radius of the wire calculated as

$$I = \frac{\pi}{4} r^4 . \quad (14)$$

For a conservative estimate modulus of elasticity, E , of $50 \cdot 10^9 \text{ N/M}^2$ for glass [33], the maximum deflection, v_{max} , is calculated as

$$v_{\max} = -\frac{FL^3}{3EI} . \quad (15)$$

The results from the calculations are shown in Tables 5.1 and 5.2.

Table 5.1. The Worst Case Deflection Calculations for the Prototype Wire Feeder. As the Wire Feeder Was Only Able to Feed 0.5 mm and 1mm wire the Greyed Out Sections are Purely Theoretical.

Prototype Wire Feeder 6cm standoff distance			
Wire Diameter (mm)	Viscous Force (N)	Area Moment of Inertia (m ⁴)	Maximum Deflection (mm)
0.125	0.001963495	1.19842E-17	235.9296
0.5	0.007853982	3.06796E-15	3.6864
1	0.015707963	4.90874E-14	0.4608
1.25	0.019634954	1.19842E-13	0.2359296
1.5	0.023561945	2.48505E-13	0.136533333
2	0.031415927	7.85398E-13	0.0576

Table 5.2. The Worst Case Deflection Calculations for the New Wire Feeder.

Updated Wire Feeder 10mm standoff distance		
Wire Diameter (mm)	Maximum Deflection (mm)	Percent Decrease in deflection
0.125	1.092266667	21500%
0.5	0.017066667	21500%
1	0.002133333	21500%
1.25	0.001092267	21500%
1.5	0.000632099	21500%
2	0.000266667	21500%

This shows that the new wire feeders are able to decrease deflection by 2 orders of magnitude. While the new wire feeders are able to feed 0.125 mm wire, and the system is able to print 0.125 mm wire, the deflection of the wire due to the viscous effects of the melt pool causes many parts to fail. No such difficulties have been found with the other reported wire diameters.

The third and fourth goals were to have variable tension springs and to create a feeding mechanism that limits the amount of wire breakage, both of which were accomplished. Previously, the system would break between two or three filaments per piece. The resulting design breaks wires so rarely that none have been reported.

The fifth goal was to allow the wire feeders to be aligned repeatedly and quickly. This was achieved by getting rid of the extra degree of freedom the old wire feeders had, and mounting the new wire feeders to a Z stage and a rotational stage.

The sixth goal was to use a motor with a higher resolution than the original stepper motors. The Yaskawa motors have a resolution of 0.0027° compared to the original stepper motors which had a resolution of 1.8° and a functional resolution of 22.5° . The velocity of the Yaskawa motors does not track the reference well, as seen in Section 5. The average velocity it produces is within 2% as seen in Table 5.3.

Table 5.3. Average Feeder Velocity Response to a Reference Velocity.

Yaskawa Controller Response		
Reference Velocity (mm/s)	Average Velocity (mm/s)	Percent Difference
0.5	0.4895	2.10%
1	0.9948	0.52%
2	2.0015	0.08%
5	4.9597	0.81%
10	10.0393	0.39%
20	19.9897	0.05%

The seventh goal was to acquire a laser capable of melting quartz and alumina that is both controllable and observable. The Synrad 125 CO₂ laser meets all of these requirements while also being more stable than the air cooled GEM-100.

The eighth goal was to incorporate a set of stages that were controllable and observable. They also had to have a high resolution, as well as be able to operate under the load of the heater and the AM glass pieces. The Aerotech stages met these design requirements as they have a resolution of 10nm, and a load capacity of 10kg. The stages, when tuned, all had a time constant below 0.003 s⁻¹ with zero steady state error. The percent overshoot, settling time and time constants are shown in Table 5.4. The settling time, time constants, and percent overshoot, are all acceptable for the current Glass AM process.

Table 5.4. Aerotech Stage Controller Response.

Aerotech Controller Response				
	Time Constant (s)	Over Shoot (%)	Settling Time (s)	Steady State Ramp Error (μm)
X stage	0.0027	11.05%	0.011	2.31
Y stage	0.0027	23.55%	0.030	1.04
Z stage	0.0025	19.00%	0.007	0.81

The ninth goal, replacing the strip heater with a heater that was controllable and observable, and able to reach the annealing temperature of quartz was not quite reached. The Watlow heater is controllable and observable, but it is not able to reach the annealing

temperature of quartz. This has not been observed to be a problem for quartz as quartz has a low thermal expansion coefficient [31, 32].

The final goal was to create a system that is more user friendly, takes less maintenance, and cuts down the amount of setup and production time. This goal has been reached. On the prototype system printing a 1D wall took 20 minutes from set up to completion. The new system is able to print the same wall in 5 minutes, with a better morphology thanks to the path planning software, and the shutter. An example of a wall made on the prototype system and a wall made on the new system is shown in Figure 5.1. More complex geometries can also be made on the new system, like the pyramid shown in Figure 5.2.

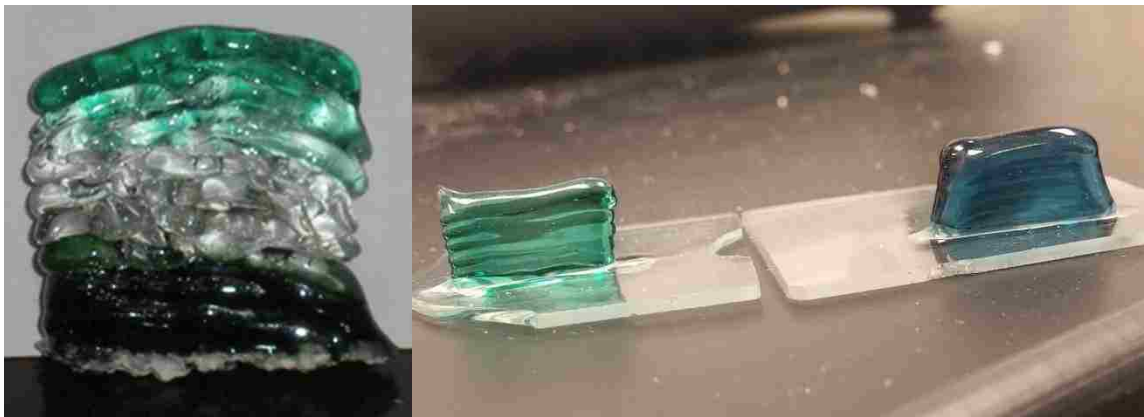


Figure 5.1. Wall Made with Prototype System and Hand Feeding on the Left, and Two Walls Printed on the New Glass AM system on the Right.



Figure 5.2. 3D Printed Soda-Lime Glass Pyramid.

6. SUMMARY AND CONCLUSION

This thesis has shown that, while there has been significant advancement in additive manufacturing for structural parts, AM of transparent parts has not kept up the same pace. This is because it is difficult to make transparent parts, as even small gas inclusions can render translucent parts opaque. Even less work has been done on the AM of Glass. This is due to the high melting temperature of glass, and because most glass AM processes are only able to produce opaque glass that are not fully dense rendering them useless for optical purposes. Only two processes exist that are able to produce transparent glass parts: an extrusion process which is used to create art pieces, and a novel wire fed process. The wire fed process is explained in detail, and the prototype system used to fine tune the process is described, the design flaws are expounded upon, and new design goals are set. The design process and experimental set up are described in detail. The wire feeder's design, in particular, is discussed as the design challenges associated with the wire feeder are the leading limitations of the process. These include: closeness to the melt pool, wire diameter robustness, and wire breakage.

A spring damper model of the system is analytically derived by assuming that the forces in the melt pool are purely viscous and the mass is negligible. This model consists of an input and output, as well as two disturbances, the location of the solidification front, and the location of the front of the melt pool. The control scheme was also discussed. The stages are controlled using PID controllers with the derivative calculated using a backwards difference Euler approximation. The wire feeders are controlled with a weak PI controller as the nonlinear dominant cogging forces cause the velocity to change too drastically and adding a derivative gain drives the system unstable.

The new system has proven to be able to significantly improve the morphology of the Glass AM system, and cut the time it takes to manufacture glass pieces to a quarter of the previous time it took. The amount of broken wires has decreased to a negligible number, and the system has been able to create AM glass with optical properties identical to that of cast glass. The creation of the new system has also provided a platform for improvement. These improvements include feeding single mode fiber optic cable and creating a process controller to keep errors from propagating in the layer-to-layer domain.

7. FUTURE WORK AND LIMITATIONS

The goal of this work was to outline the design and construction of an automated system for additively manufacturing glass. Automating the process is the first step to creating a system with which optical glasses can be created, but there are many avenues for future work that will improve the system further.

As the printing process is a novel process there is still room for improvement in the mechanical systems, electrical systems, and software systems. One such improvement is the feeding of the 0.125 mm optical fiber. While the feeders are able to feed the optical fiber into the melt pool and deposit tracks of it, 10mm is still too far from the melt pool to keep the wire from wondering within a millimeter of the nominal position. To solve this problem, the wire feeder will have to reach closer still to the melt pool. A proposed solution is to use either a 30 or 31 gauge hypodermic needle attached to a modified feeder clamp plate. This should allow the feeder to get within a millimeter of the melt pool and restrict the deflection of the wire to a micron.

The Yaskawa motors, while they have a very high resolution, are velocity controlled with relatively weak controllers. This is due to the fact that the motors have very large nonlinear cogging forces which act as the dominate force in the wire feeder. In order to get a better performance out of the wire feeders, an iterative learning filter can be used to create a cogging map. This type of controller is much more complex than a standard PID controller and would require running the motors in an absolute mode that finds its zero position, like the stages, before the system can enter normal operation mode. These motors can also be replaced with motors that are made to handle smaller

loads, though this would take a redesign of the feeders, and the electrical cabinet which houses the feeder amplifiers

The Aerotech stages use standard PID controllers where the derivative is calculated as an Euler backwards approximation. As seen in Section 5, this provides a good base line performance for the stages allowing the stages to drive the error between the commanded position and the actual position below 10 microns in 0.1 seconds. However this performance can be increased by adding a low pass filter on the derivative of the error, as the Euler approximation can be very noisy, and by adding a feed forward acceleration gain to the control.

Furthermore, it has been observed that even with good controllers in the time domain, errors can propagate in the layer-to-layer domain as observed by Sammons et al. [36]. In order to have a system that is capable of reaching the strict tolerances of optical devices, further modeling must be done by exciting the system with a pseudo random binary signal. This will allow a layer-to-layer controller to be created in the method outlined by Sammons et al. to keep the propagation of layer to layer errors at a minimum.

This full process controller will work best if it has feedback with which to measure the system. For this purpose, the thermopile used to measure the laser power, and the spectrometer, used to measure the emittance of the melt pool may be added to the controlling program. Similarly, control of the laser power and substrate heater in situ would also add another level of controllability to the process.

There also exists an abundance of research possibilities about the process, which may include controlling the cooling rate of glasses to keep glasses from crystalizing, observing and predicting melt pool dynamics when glasses are mixed, investigating how

cooling rates affect thermally induced stresses using birefringence, predicting and minimizing periodic bubble formation, and of course designing GRIN and Transformation optics.

The largest limiting factor of the Glass AM process is the length of filaments used. The length of the filaments directly limits the size of continuous glass pieces that can be made. For small glass pieces, this is not a problem, as one glass filament contains enough material to make one continuous part. In contrast, the process for larger parts must be interrupted so new filaments can be loaded into the feeder. The most promising solution to this problem is to use single or multi-multimode fiber optic fibers. These fibers are sold by the kilometer and are very high optical quality glasses. In order to use these fibers the glass must be stripped of its plastic coating. Some experiments have been conducted using acetone to remove the coating, but a full scale automated stripping and spooling process has not been created.

APPENDIX A.

PATH GENERATION CALCULATIONS

In order to calculate the reference signal for a linear motion, the acceleration and the velocity vector components must be calculated. The reference velocity, the reference acceleration, and the initial and final positions are supplied by the user. To calculate the acceleration vector components and the velocity vector components the position vector, p , is calculated from the final position (x_f, y_f, z_f) and the initial position vector (x_i, y_i, z_i) such that,

$$\bar{p} = ((x_f - x_i), (y_f - y_i), (z_f - z_i)) . \quad (16)$$

The magnitude of the position vector is then found by taking the l_2 norm,

$$\|\bar{p}\| = \sqrt{((x_f - x_i)^2 + (y_f - y_i)^2 + (z_f - z_i)^2)} . \quad (17)$$

Using this magnitude, the unit vector is found by dividing each component of (16) by the scalar value (17),

$$\bar{u} = \left(\frac{(x_f - x_i)}{\|\bar{p}\|}, \frac{(y_f - y_i)}{\|\bar{p}\|}, \frac{(z_f - z_i)}{\|\bar{p}\|} \right) = (\hat{x}, \hat{y}, \hat{z}) . \quad (18)$$

The absolute value of each of these vectors is taken. This is done because the Linear Segment Polynomial Blend (LSPB) constant acceleration reference generator assigns the direction of motion based off of the position vector in later steps.

$$|\bar{u}| = (|\hat{x}|, |\hat{y}|, |\hat{z}|) \quad (19)$$

At this point, the given magnitude of the acceleration or velocity, M , is multiplied through all of the individual vector components in (4) resulting in the three vector components.

$$M \cdot |\bar{u}| = (M_x, M_y, M_z) . \quad (20)$$

The vector components of the velocity and acceleration are then passed to the LSPB reference generator. For a single axis these components are designated as the reference velocity V_r , and the reference acceleration A_r . The discrete time step dt , the final position P_f and the initial position P_i are also necessary to generate the trajectory. The first step to finding the trajectory is to find the number of iterations in the first phase I_1 , the acceleration phase, which is calculated as,

$$\text{Ceil} \left(\frac{\frac{V_r}{A_r}}{dt} \right) = I_1. \quad (21)$$

The *Ceil* function forces the acceleration phase to fall inside an integer number of iterations. From this point the time it takes to complete phase one, T_1 , can be calculated as,

$$I_1 \cdot dt = T_1. \quad (22)$$

Similarly the number of iterations in the second phase I_2 , the constant velocity phase, can be found using,

$$\text{Ceil} \left(\frac{\frac{|P_f - P_i|}{V_r}}{dt} \right) = I_2, \quad (23)$$

and the amount of time to complete the second iteration, T_2 , can be calculated the same way that T_1 was calculated in (22)

$$I_2 \cdot dt = T_2. \quad (24)$$

Since the reference velocity may take a non-integer number of iterations to reach the final position, a new slightly adjusted velocity, V_{mew} must be calculated which will enable the stage to reach the final position in an integer number of iterations

$$V_{mew} = \frac{|P_f - P_i|}{T_2} \quad (25)$$

The actual velocity, V_2 , during phase two, the constant velocity phase, is direction dependent on the direction of the position vector and must therefore be calculated as

$$V_2 = \text{sgn}(P_f - P_i)V_{mew} \quad (26)$$

Similar to the velocity, a slightly adjusted acceleration must be calculated so that the acceleration and deceleration phases are able to be completed in an integer number of iterations. This new acceleration, A_{mew} , is calculated as,

$$A_{mew} = \frac{V_{mew}}{T_1} \quad (27)$$

The actual accelerations, A_1 and A_3 , during phases one and three, the acceleration phase and deceleration phase, is direction dependent on the direction of the position vector and must therefore be calculated as,

$$A_1 = \text{sgn}(P_f - P_i)A_{mew}, \quad (28)$$

and

$$A_3 = -\text{sgn}(P_f - P_i)A_{mew} \quad (29)$$

So long as $I_1 < I_2$, and the iteration, i , $i \leq I_1 + 1$, as LabVIEW indexes at 1, the position at any iteration $P(i)$ can be calculated as

$$P(i) = P_i + \frac{A_1 t(i)^2}{2} \quad (30)$$

In the case that $I_1 < I_2$ and $I_2 + 1 > i \geq I_1 + 1$, the position can be calculated as

$$P(i) = P_i + V_2(t(i) - T_1) + \frac{A_1 T_1^2}{2} \quad (31)$$

In the case that $I_1 < I_2$, and $i \geq I_2 + 1$ the position can be calculated as

$$P(i) = P_i - V_2 T_1 + (V_2 - A_3 T_2)t(i) + \frac{A_1 T_1^2}{2} + \frac{A_3(t(i)^2 + T_2^2)}{2} \quad (32)$$

When $i \geq I_1 + I_2 + 1$ the final position has been reached. This means that

$$P(i) = P(i-1) \quad (33)$$

until a new reference position has been given.

There is a second case that may occur that is not addressed by the above equations. A reference acceleration could be designated by the user that will not be able to reach the designated velocity before the system has gone half way to the final point. This condition is found when $I_2 < I_1$. The velocity curve of this condition has two phases, an acceleration and deceleration phase, which changes at the critical time T_c . T_c occurs when the stage is half way to the final position or,

$$P_i + \frac{A_r T_c^2}{2} = \frac{|P_f - P_i|}{2} + P_i \quad (34)$$

Simplifying (34),

$$A_r T_c^2 = |P_f - P_i| \quad (35)$$

yields

$$T_c = \sqrt{\frac{|P_f - P_i|}{A_r}} \quad (36)$$

The number of iterations, I_c , it takes to reach this critical time can be calculated as

$$\text{Ceil}\left(\frac{T_c}{dt}\right) = I_c \quad (37)$$

Similar to (21) and (23) the number of iterations must be rounded up to the nearest integer. The new critical time T_{cnew} is calculated as

$$T_{cnew} = I_c dt \quad (38)$$

The new acceleration is calculated as

$$A_{cnew} = \frac{|P_f - P_i|}{T_{cnew}^2} \quad (39)$$

and the acceleration for the first phase A_{c1} and the deceleration for phase two A_{c2} are calculated as

$$A_{c1} = \text{sgn}(P_f - P_i)A_{cnew} \quad (40)$$

and

$$A_{c2} = -\text{sgn}(P_f - P_i)A_{cnew} \quad (41)$$

The acceleration phase occurs when $i \leq I_c$.

The position reference is calculated using calculus where $A(i)$ is the acceleration for any iteration, $V(i)$ is the velocity at any iteration, and $P(i)$ is the position for any given iteration. By integrating

$$A(i) = A_1 \quad (42)$$

with an initial velocity of zero the velocity is found to be

$$V(i) = A_1 t(i) \quad (43)$$

Integrating a second time with the initial position, P_i , as the boundary condition the position is found to be

$$P(i) = P_i + \frac{A_1 t(i)^2}{2} . \quad (44)$$

The acceleration, velocity, and position can be calculated for $I_c < i < 2I_c$ as

$$A(i) = A_2 , \quad (45)$$

$$V(i) = A_1 t_c + A_2 t(i) , \quad (46)$$

and

$$P(i) = P_i + \frac{A_1 t_c^2}{2} + A_1 t_c (t(i) - t_c) + \frac{A_2 (t(i) - t_c)^2}{2} . \quad (47)$$

If

$$i \geq 2I_c , \quad (48)$$

then

$$P(i) = P(i-1) . \quad (49)$$

In order to move in a circular motion, one needs to know the initial position, the final position, the velocity, the acceleration and the X and Y offset. Once these things are known, the initial and final angles are calculated, and a linear trajectory of the angles is calculated as outlined above. Given the X and Y offset, I and J , it is possible to calculate the radius of the generated path as,

$$r = \sqrt{I^2 + J^2} . \quad (50)$$

The angle between the x axis and the center of the circle, or the initial angle, θ_i , is calculated as

$$\theta_i = \arctan 2 \left(\frac{J}{I} \right) \quad (51)$$

As $\arctan 2$ is only defined between $[-\pi, \pi]$, if

$$\theta_i < 0 , \quad (52)$$

then

$$\theta_i = \theta_i + 2\pi \quad (53)$$

Similarly the final angle θ_f is calculated as

$$\theta_f = \arctan 2 \left(\frac{(Y_f + J - Y_i)}{(X_f + I - X_i)} \right) \quad (54)$$

If

$$\theta_f < 0 \quad (55)$$

then

$$\theta_f = \theta_f + 2\pi \quad (56)$$

The angular acceleration, α , and the angular velocity, ω , can be calculated given the commanded acceleration, a , and the commanded velocity, v , as

$$\alpha = \frac{a}{r} \quad (57)$$

and

$$\omega = \frac{v}{r} \quad (58)$$

Figure A1.1 shows the logic necessary to decide how to calculate the final angle, θ_f , for a circular motion. This calculation is necessary as atan2 is only valid from $[-\pi, \pi]$. For instance if θ_f was calculated as -5° from the x axis initially, and a clockwise motion to 0° was desired, 360° would need to be added to θ_f to create the desired motion. With all edge cases included, there are 6 possible calculations for θ_f . Figure A1.1 shows a logic tree which outlines which θ_f to use for a desired movement

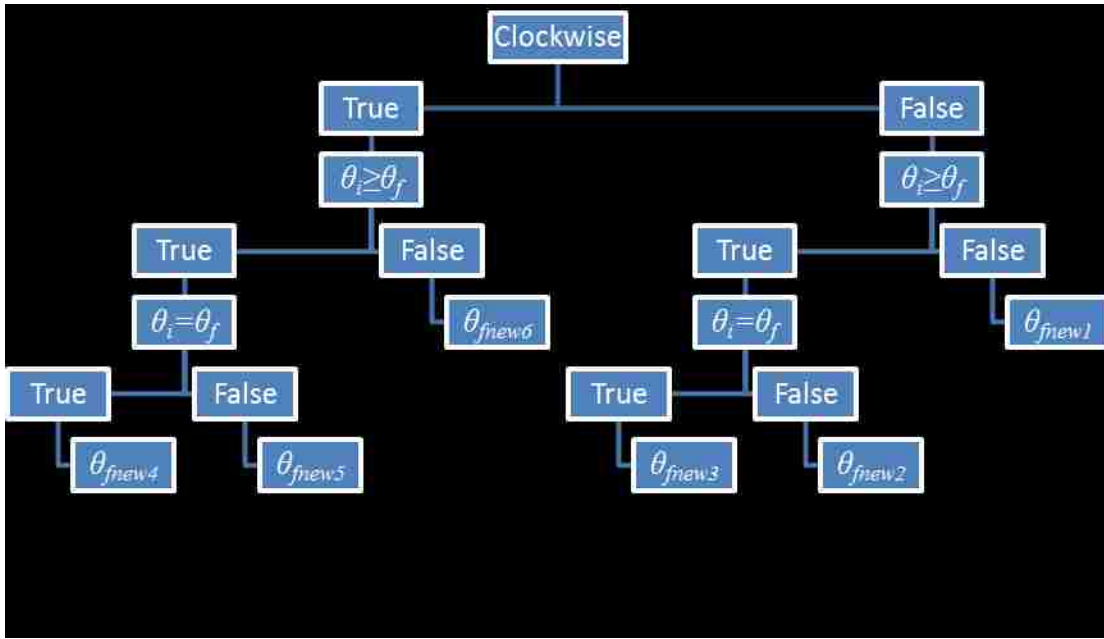


Figure A1.1. θ_f calculation logic.

θ_{fnew} 1,2,3,4,5, and 6 are calculated as

$$\theta_{fnew1} = \theta_f , \quad (59)$$

$$\theta_{fnew2} = \theta_f + 2\pi , \quad (60)$$

$$\theta_{fnew3} = \theta_f , \quad (61)$$

$$\theta_{fnew4} = \theta_f - 2\pi , \quad (62)$$

$$\theta_{fnew5} = \theta_f , \quad (63)$$

and

$$\theta_{fnew6} = (\theta_i - 2\pi) + (\theta_f - \theta_i) . \quad (64)$$

These new θ_f 's are then fed into the LSPB, along with the angular velocity, angular acceleration, the time step size, and θ_i . The LSPB returns the iterative angle $\theta(i)$ and $\theta(i)$ is then used to calculate the iterative position $X(i)$ and $Y(i)$ using,

$$Y(i) = Y_i + J - r \cdot \sin(\theta(i)) \quad (65)$$

$$X(i) = X_i + I - r \cdot \cos(\theta(i)) \quad (66)$$

APPENDIX B.
ERROR HANDLING

There are five possible faults that can occur in the Glass AM system. These faults include: an over speed fault, an end of software limit fault, an end of hardware position fault, an external error fault, an excessive voltage fault, and an excessive error fault. The subroutine that is used to check for these faults is used twice for each stage and motor in two different modes. The first mode is used when the stages are homing in velocity mode. The subroutine only checks for excessive voltage fault, external error fault, and hardware limit faults, as the stages relative position is unknown.

To generate the over speed fault, the velocity, v_k , must be calculated from the current position, x_k , the last position, x_{k+1} , and the time step, Δt , using Euler's backwards difference approximation method,

$$v_k = \frac{x_k - x_{k+1}}{\Delta t} . \quad (67)$$

The error is generated when given a user specified velocity v_{\max} ,

$$v_k > v_{\max} . \quad (68)$$

The end of software limit fault takes a maximum user specified position x_{\max} , and a minimum user specified position x_{\min} , and if the current position, x_k , is

$$x_{\min} > x_k , \quad (69)$$

or,

$$x_{\max} < x_k , \quad (70)$$

The overvoltage (over current) fault is calculated using a low pass filter with a user designated settling time. The control signal, u_k , is squared to account for negative voltages. The maximum allowable time at the maximum continuous current, t , also doubles as the low pass's settling time, which sets the cut off frequency of the filter at $\frac{1}{t}$.

The time step, Δt , is also needed to calculate the filtered root mean squared value of the control, y_k , as

$$y_k = \left(1 - \frac{\Delta t}{.25t}\right) y_{k-1} + u_k^2 \frac{\Delta t}{.25t} \quad (72)$$

If the maximum control value, u_{\max} , is

$$.98u_{\max} \leq y_k, \quad (73)$$

then the over volt fault is activated.

The last type of fault is the excessive error fault. The error, E_k , is calculated when given the reference signal, R_k , and the position, x_k ,

$$E_k = |R_k - x_k|, \quad (74)$$

if

$$E_k > 0.02, \quad (75)$$

then the excessive error fault will be triggered. The parameters chosen for each mode of operation are shown in Tables 1-3.

Table A2.1. User Designated Safety Parameters for the Stages While in Velocity Mode.
The Greyed Out Areas Are Not Applicable to The System While in Velocity Mode.

Velocity Mode-Stages	
Error Type	User Designated Parameters
Over Speed	$v_{\max}=10 \text{ mm/s}$
Software Limit	
Excessive Error	
Over Volt	$u_{\max}=3 \text{ v}, t=0.3 \text{ s}$

Table A2.2. User Designated Safety Parameters for the Wire Feeders While in Velocity Mode. The Greyed Out Areas Are Not Applicable to the System While in Velocity Mode.

Velocity Mode-Wire Feeders	
Error Type	User Designated Parameters
Over Speed	$v_{max}=10 \text{ mm/s}$
Software Limit	
Excessive Error	
Over Volt	$u_{max}=3 \text{ v}, t=0.3 \text{ s}$

Table A2.3. User Designated Safety Parameters for the Stages While in Position Mode. As the Relative Location of the Stages is Known and a Reference Signal is Generated, The Software Limit Fault is Applicable as is the Excessive Error Fault.

Position Mode-Stages	
Error Type	User Designated Parameters
Over Speed	$v_{max}=10 \text{ mm/s}$
Software Limit	$x_{max}=60 \text{ mm}, x_{min}=-60 \text{ mm},$ $y_{max}=60 \text{ mm}, y_{min}=-60 \text{ mm},$ $z_{max}=1 \text{ mm}, z_{min}=-150 \text{ mm}$
Excessive Error	0.02 mm
Over Volt	$u_{max}=3 \text{ v}, t=0.3 \text{ s}$

BIBLIOGRAPHY

- [1] Moore, D. T., 1980, "Gradient-index optics: a review," *Applied Optics*, 19(7), pp.1035-1038.
- [2] Niino, T., and Yamada, H., 2009, "Fabrication of Transparent Parts by Laser Sintering Process-Transparentization of laser sintered plastic parts by infiltrating thermosetting epoxy with tuned refractive index," *Journal of the Japan Society for Precision Engineering*, 75(12), pp. 1454-1458.
- [3] Marder, S. R., Brédas, J.-L., and Perry, J. W., 2007, "Materials for multiphoton 3D microfabrication," *Mrs Bulletin*, 32(07), pp. 561-565.
- [4] Li, Y., Gargiulo, E. P., and Keefe, M., 2000, "Studies in direct tooling using stereolithography," *Transactions-American Society of Mechanical Engineers Journal of Manufacturing Science and Engineering*, 122(2), pp. 316-322.
- [5] Derby, B., 2010, "Inkjet printing of functional and structural materials: fluid property requirements, feature stability, and resolution," *Annual Review of Materials Research*, 40, pp. 395-414.
- [6] Hutmacher, D. W., Schantz, T., Zein, I., Ng, K. W., Teoh, S. H., and Tan, K. C., 2001, "Mechanical properties and cell cultural response of polycaprolactone scaffolds designed and fabricated via fused deposition modeling," *Journal of biomedical materials research*, 55(2), pp. 203-216.
- [7] Urness, A. C., Moore, E. D., Kamysiak, K. K., Cole, M. C., and McLeod, R. R., 2013, "Liquid deposition photolithography for submicrometer resolution three-dimensional index structuring with large throughput," *Light Sci Appl*, 2, p. e56.
- [8] Brockmeyer, E., Poupyrev, I., and Hudson, S., 2013, "PAPILLON: designing curved display surfaces with printed optics," *Proceedings of the 26th annual ACM symposium on User interface software and technology*, ACM, St. Andrews, Scotland, United Kingdom, pp. 457-462.
- [9] Willis, K., Brockmeyer, E., Hudson, S., and Poupyrev, I., 2012, "Printed optics: 3D printing of embedded optical elements for interactive devices," *Proceedings of the 25th annual ACM symposium on User interface software and technology*, ACM, Cambridge, Massachusetts, USA, pp. 589-598.
- [10] Weber, M. J., 2002, *Handbook of optical materials*, CRC press.

- [11] Huang, Y., Leu, M. C., Mazumder, J., and Donmez, A., 2015, "Additive Manufacturing: Current State, Future Potential, Gaps and Needs, and Recommendations," *Journal of Manufacturing Science and Engineering*, 137(1), pp. 014001-014001.
- [12] Khmyrov, R., Grigoriev, S., Okunkova, A., and Gusarov, A., 2014, "On the possibility of selective laser melting of quartz glass," *Physics Procedia*, 56, pp. 345-356.
- [13] Khmyrov, R. S., Protasov, C. E., Grigoriev, S. N., and Gusarov, A. V., 2015, "Crack-free selective laser melting of silica glass: single beads and monolayers on the substrate of the same material," *The International Journal of Advanced Manufacturing Technology*, pp. 1-9.
- [14] Klocke, F., McClung, A., and Ader, C., "Direct laser sintering of borosilicate glass," *Proc. Solid Freeform Fabrication Symposium Proceedings*, Austin, TX, Aug, pp. 3-5.
- [15] Luo, J., Pan, H., and Kinzel, E. C., 2014, "Additive Manufacturing of Glass," *Journal of Manufacturing Science and Engineering*, 136(6), pp. 061024-061024.
- [16] Baillis, D., Pilon, L., Randrianalisoa, H., Gomez, R., and Viskanta, R., 2004, "Measurements of radiation characteristics of fused quartz containing bubbles," *J. Opt. Soc. Am. A*, 21(1), pp. 149-159.
- [17] Pilon, L., and Viskanta, R., 2003, "Radiation characteristics of glass containing gas bubbles," *Journal of the American Ceramic Society*, 86(8).
- [18] Klein, J., Stern, M., Franchin, G., Kayser, M., Inamura, C., Dave, S., Weaver, J. C., Houk, P., Colombo, P., and Yang, M., 2015, "Additive Manufacturing of Optically Transparent Glass," *3D Printing and Additive Manufacturing*, 2(3), pp. 92-105.
- [19] Klein, S., Simske, S., Adams, G., Parraman, C., Walters, P., Huson, D., and Hoskins, S., "3D Printing of Transparent Glass," *Proc. NIP & Digital Fabrication Conference, Society for Imaging Science and Technology*, pp. 336-337.
- [20] Marchelli, G., Prabhakar, R., Storti, D., and Ganter, M., 2011, "The guide to glass 3D printing: developments, methods, diagnostics and results," *Rapid Prototyping Journal*, 17(3), pp. 187-194.
- [21] Mok, S. H., Bi, G., Folkes, J., Pashby, I., and Segal, J., 2008, "Deposition of Ti-6Al-4V using a high power diode laser and wire, Part II: Investigation on the mechanical properties," *Surface and Coatings Technology*, **202**(19), pp. 4613-4619.

- [22] Martina, F., Mehnen, J., Williams, S. W., Colegrove, P., and Wang, F., 2012, "Investigation of the benefits of plasma deposition for the additive layer manufacture of Ti-6Al-4V," *Journal of Materials Processing Technology*, 212(6), pp. 1377-1386.
- [23] Heralić, A., Christiansson, A.-K., and Lennartson, B., 2012, "Height control of laser metal-wire deposition based on iterative learning control and 3D scanning," *Optics and Lasers in Engineering*, 50(9), pp. 1230-1241.
- [24] Syed, W. U. H., and Li, L., 2005, "Effects of wire feeding direction and location in multiple layer diode laser direct metal deposition," *Applied Surface Science*, 248(1), pp. 518-524.
- [25] Mok, S. H., Bi, G., Folkes, J., and Pashby, I., 2008, "Deposition of Ti-6Al-4V using a high power diode laser and wire, Part I: Investigation on the process characteristics," *Surface and Coatings Technology*, 202(16), pp. 3933-3939.
- [26] Heralić, A., Christiansson, A.-K., Ottosson, M., and Lennartson, B., 2010, "Increased stability in laser metal wire deposition through feedback from optical measurements," *Optics and Lasers in Engineering*, 48(4), pp. 478-485.
- [27] Xiong, J., and Zhang, G., 2014, "Adaptive control of deposited height in GMAW-based layer additive manufacturing," *Journal of Materials Processing Technology*, 214(4), pp. 962-968.
- [28] Katou, M., Oh, J., Miyamoto, Y., Matsuura, K., and Kudoh, M., 2007, "Freeform fabrication of titanium metal and intermetallic alloys by three-dimensional micro welding," *Materials & design*, 28(7), pp. 2093-2098.
- [29] Luo, J., Gilbert, L. J., Qu, C., Wilson, J., Bristow, D., Landers, R., and Kinzel, E., "Wire-Fed Additive Manufacturing of Transparent Glass Parts," *Proc. ASME 2015 International Manufacturing Science and Engineering Conference*, American Society of Mechanical Engineers, pp. V001T002A108-V001T002A108.
- [30] Luo, J., Gilbert, L. J., Qu, C., Landers, R., Bristow, D., and Kinzel, E., 2016, "Additive manufacturing of transparent soda-lime glass using a filament-fed process," Submitted to *Journal of Manufacturing Science and Engineering*.
- [31] Luo, J., Gilbert, L., Qu, C., Morrow, B., Bristow, D., Landers, R., Goldstein, J., Urbas, A., and Kinzel, E., 2015, "Solid freeform fabrication of transparent fused quartz using a filament fed process," *Annual International Solid Freeform Fabrication Symposium*, D. Bourell, ed., University of Texas, Austin, TX, pp. 122-133.

- [32] Luo, J., Gilbert, L. J., Bristow, D. A., Landers, R. G., Goldstein, J. T., Urbas, A. M., and Kinzel, E. C., "Additive manufacturing of glass for optical applications," pp. 97380Y-97380Y-97389.
- [33] 2016 "The Engineering Toolbox: Modulus of Elasticity or Young's Modulus - and Tensile Modulus for some common Materials," from http://www.engineeringtoolbox.com/young-modulus-d_417.html.
- [34] Luo, J., Gilbert, L. J., Peters, C.D., Bristow, D. A., Landers, R. G., Goldstein, J., Urbas, A., and Kinzel, E. C., "Bubble formation study in additive manufacturing of glass," 2016 SPIE DSS Conference, Baltimore, MD.
- [35] Shelby, J. E., Lopes, Maria, 2005, Introduction to glass science and technology, Royal Society of Chemistry. <http://dx.doi.org/10.1039/9781847551160>.
- [36] Sammons, P. M., Bristow, D. A., and Landers, R. G., 2013, "Height dependent laser metal deposition process modeling," *Journal of Manufacturing Science and Engineering*, 135(5), p. 054501.

VITA

Luke Gilbert was born November 14, 1991. He graduated from Blue Springs High School in 2010, and received his B.S. in Mechanical Engineering, Summa Cum Laude, from Missouri University of Science and Technology in 2014. During his graduate studies he worked with the Precision Motion Control Laboratory, the Thermal Radiation Laboratory, on glass additive manufacturing, and co-authored five conference papers and two journal papers. In July 2016 he received his Master of Science degree in Mechanical Engineering from Missouri University of Science and Technology.